Article

SOURCE DATA | TRANSPARENT PROCESS | OPEN ACCESS

THE EMBO JOURNAL

Astrogenesis in the murine dentate gyrus is a life-long and dynamic process

Julia Schneider[1], Johannes Weigel[1], Marie-Theres Wittmann[1,2], Pavel Svehla[3,4,5], Sebastian Ehrt[3,5], Fang Zheng[6], Tarek Elmzzahi[1,7], Julian Karpf[1], Lucía Paniagua-Herranz[8,9,10], Onur Basak[11], Arif Ekici[2], Andre Reis[2], Christian Alzheimer[6], Felipe Ortega de la O[8,9,10], Sabine Liebscher[3,4,5,12] & Ruth Beckervordersandforth[1,*]

Abstract

Astrocytes are highly abundant in the mammalian brain, and their functions are of vital importance for all aspects of development, adaption, and aging of the central nervous system (CNS). Mounting evidence indicates the important contributions of astrocytes to a wide range of neuropathies. Still, our understanding of astrocyte development significantly lags behind that of other CNS cells. We here combine immunohistochemical approaches with genetic fate-mapping, behavioural paradigms, single-cell transcriptomics, and *in vivo* two-photon imaging, to comprehensively assess the generation and the proliferation of astrocytes in the dentate gyrus (DG) across the life span of a mouse. Astrogenesis in the DG is initiated by radial glia-like neural stem cells giving rise to locally dividing astrocytes that enlarge the astrocyte compartment in an outside-in-pattern. Also in the adult DG, the vast majority of astrogenesis is mediated through the proliferation of local astrocytes. Interestingly, locally dividing astrocytes were able to adapt their proliferation to environmental and behavioral stimuli revealing an unexpected plasticity. Our study establishes astrocytes as enduring plastic elements in DG circuits, implicating a vital contribution of astrocyte dynamics to hippocampal plasticity.

Keywords astrocytes; astrogenesis; adult neurogenesis; neural stem cells; voluntary exercise

Subject Categories Neuroscience

DOI 10.15252/embj.2021110409 | Received 10 December 2021 | Revised 25 March 2022 | Accepted 30 March 2022 | Published online 22 April 2022

The EMBO Journal (2022) 41: e110409

Introduction

Development, function, and plasticity of neural networks require a fine-tuned orchestration of neurons and glial cells, each of which contributes about 50% to the total cell number of the brain (Herculano-Houzel, 2014). Neurons are considered the key active components in neural circuits facilitating information processing to foster complex processes, such as learning and memory, cognition, and mood through the propagation of electrical signals. Astrocytes, together with oligodendrocytes, belong to the class of macroglia and are vital players regulating the brain's metabolism, ion homeostasis, and the cross-talk to the periphery by contributing to the formation of the blood–brain barrier (Barres, 2008; Verkhratsky & Nedergaard, 2018). In recent years, it has become evident that astrocytes are in fact more than simply passive bystanders in the brain, but they actively contribute to information processing, by shaping and regulating synaptic connectivity and plasticity, as well as by releasing neurotransmitters and gliotransmitters themselves (Ballabh *et al*, 2004; Attwell *et al*, 2010; Eroglu & Barres, 2010; Araque *et al*, 2014; Chung *et al*, 2016). Several lines of evidence argue for an important contribution of astrocytes to neuropsychiatric and neurodegenerative diseases (Verkhratsky & Parpura, 2016). In sharp contrast to neurons and oligodendrocytes, and despite the astrocytes importance and abundance in the CNS, very little is known about how astrocytes are generated. Astrogenesis has almost exclusively been studied in the developing cortex and spinal cord (Ge *et al*, 2012; Tien *et al*, 2012; Shen *et al*, 2021), where embryonic neural stem cells (NSCs) called radial glia cells give rise first to neurons and then to glia cells. This so-called neurogenic-to-gliogenic switch occurs during late embryonic development [embryonic day 16.5 (E16.5);

1 Institute of Biochemistry, Friedrich-Alexander-Universität Erlangen-Nürnberg, Erlangen, Germany
2 Institute of Human Genetics, University Hospital Erlangen, Friedrich-Alexander-Universität Erlangen-Nürnberg, Erlangen, Germany
3 Institute of Clinical Neuroimmunology, Klinikum der Universität München, Ludwig-Maximilians University Munich, Munich, Germany
4 Graduate School of Systemic Neurosciences, Ludwig-Maximilians University Munich, Munich, Germany
5 Medical Faculty, BioMedical Center, Ludwig-Maximilians University Munich, Munich, Germany
6 Institute of Physiology and Pathophysiology, Friedrich-Alexander-Universität Erlangen-Nürnberg, Erlangen, Germany
7 Department of Molecular Immunology in Neurodegeneration, German Centre for Neurodegenerative Diseases Bonn, Bonn, Germany
8 Department of Molecular Biology, Universidad Complutense de Madrid, Madrid, Spain
9 Instituto Universitario de Investigación en Neuroquímica (IUIN), Madrid, Spain
10 Instituto de Investigación Sanitaria San Carlos (IdISSC), Spain
11 Department of Translational Neuroscience, University Medical Centre Utrecht (UMCU), Utrecht, Netherlands
12 Munich Cluster for Systems Neurology (SyNergy), Munich, Germany
*Corresponding author. Tel: +49 91318526206; E-mail: ruth.beckervordersandforth@fau.de

(Miller & Gauthier, 2007)] and relies on tightly interlaced mechanisms, which initially repress astrogenesis during the neurogenic phase and later on promote it during peri- and postnatal life (gliogenic phase). Proper neocortical glial expansion emerges postnatally, when seemingly differentiated astrocytes divide symmetrically to generate new astrocytes (Ge *et al*, 2012; Clavreul *et al*, 2019). After postnatal development, astrogenesis decays in most brain regions and predominantly persists in neurogenic niches, specialized areas of the brain in which new neurons and glial cells are generated throughout life (Alvarez-Buylla & Lim, 2004; Bond *et al*, 2015; Kempermann *et al*, 2015). The dentate gyrus (DG) of the hippocampus is one of those neurogenic regions in the adult brain and represents an excellent model system to study the process of astrogenesis from development to aging.

The hippocampus, also known as the archicortex, emanates from the dentate neuroepithelium. At late gestational stages, a heterogeneous mixture of neural stem and precursor cells migrates away from the ventricular zone toward the hippocampal fissure, where neural progenitors accumulate and form the anlage of the future DG. At postnatal week two, proliferation becomes more restricted to the developing subgranular zone (SGZ), where radial glia-like NSCs (rNSCs) reside throughout life (Pleasure *et al*, 2000; Urbán & Guillemot, 2014). The generation and integration of new neurons into existing circuitries is a central process to hippocampal plasticity and involved in higher cognitive functions, such as learning, memory formation, and mood regulation (Ming & Song, 2011; Kempermann *et al*, 2015). Notably, adult neurogenesis has been reported across mammalian species (Patzke *et al*, 2015), but its existence in the human brain is a currently highly debated topic with conflicting results (Spalding *et al*, 2013; Boldrini *et al*, 2018; Cipriani *et al*, 2018; Sorrells *et al*, 2018; Moreno-Jiménez *et al*, 2019; Seki *et al*, 2019; Tobin *et al*, 2019; Franjic *et al*, 2022). Adult neurogenesis is highly dynamic and can be promoted by physiological stimuli, such as voluntary exercise, which significantly increases the proliferation of neural progenitor cells (van Praag *et al*, 1999b). During aging, neurogenesis gradually declines due to rNSC pool exhaustion and decreased proliferation of neuronal progenitors until it is fully ceased in aged mice (Kuhn *et al*, 1996; Seki, 2002; Bondolfi *et al*, 2004; Garcia *et al*, 2004; Heine *et al*, 2004; Encinas *et al*, 2011).

Astrocytes are key components of the hippocampal neurogenic niche, and multiple lines of evidence suggest a major impact of astrocytes on DG plasticity by positively regulating rNSCs function and neuronal maturation (Lie *et al*, 2005; Song *et al*, 2012; Ehret *et al*, 2015; Sultan *et al*, 2015; Schneider *et al*, 2019). While adult rNSCs and neurogenesis have been in the focus of attention over the last two decades, the generation of astrocytes in the archicortex is a fundamentally understudied process. Like granule neurons, dentate astrocytes originate from developmental and adult rNSCs (Berg *et al*, 2019). Neurogenesis and astrogenesis in the developing DG occur simultaneously (Bond *et al*, 2020) in analogy to what has been recently suggested for neocortical development (Shen *et al*, 2021). During adult stages, astrocytes in the DG are continuously generated either by asymmetric division or trans-differentiation from rNSCs (Bonaguidi *et al*, 2011; Encinas *et al*, 2011). With the aim to gain insights into the mechanisms governing astrogenesis, we here assessed basic principles of astrocyte generation and dynamics in the DG throughout the life span of a mouse. Our data reveal that astrocytes originated from perinatal rNSCs, which give rise to proliferating astrocytes expanding the astrocyte compartment. We observed a temporal order in the generation of astrocytes located within different DG compartments, indicating an outside-in-pattern of astrogenesis, as shown already for granule neurons (Mathews *et al*, 2010). Importantly, our data revealed that the predominant source of newborn astrocytes in the adult DG are not rNSCs, but are locally dividing niche astrocytes, which are able to adapt their proliferation in response to pro- or anti-neurogenic stimuli (voluntary exercise and aging, respectively), thus revealing an unexpectedly high level of astrocyte plasticity.

Results

Astrogenesis in the developing murine DG

To comprehensively understand how and when astrocytes are generated in the developing DG, we here combined genetic fate-mapping with thymidine analogue tracing and cell cycle marker analysis. To unambiguously determine the origin of DG astrocytes, we performed fate-mapping experiments using a tamoxifen-inducible mouse model [*Nestin*CreER^{T2}; (Yamaguchi *et al*, 2000)], in which the Cre recombinase is expressed in rNSCs. These mice were crossed to a reporter mouse line with a floxed STOP codon in front of a GFP [CAG CAT GFP; (Nakamura *et al*, 2006)] to monitor recombination events (Fig 1A). These mice will be from now on referred to as *Nestin*CreER^{T2}; GFP animals. Administration of tamoxifen allows to specifically define the timepoint at which the Cre recombinase can enter the nucleus, leading to the expression of the GFP reporter in rNSCs and their progeny. Since the first astrocytes have been reported to arise at the beginning of postnatal development (Bond *et al*, 2020), we specifically targeted perinatal rNSCs by tamoxifen administration at birth (Fig 1A and B) and analyzed their progeny at postnatal days 3 (P3), P7, P10, and P14 in distinct DG compartments, such as hilus, granular zone (GZ), and molecular layer (ML; Fig 1B). First, we specified whether the *Nestin*-CreER^{T2}; GFP mouse line is a valid tool for rNSCs lineage tracing by determining its recombination efficiency and specificity (Fig EV1A–C). The specificity (number of NESTIN$^+$/GFP$^+$ cells of all GFP$^+$ cells) was 92.61% (Fig EV1A), showing that perinatal rNSCs were the main target of our recombination strategy. Due to their high density, it was impossible to reliably count the number of NESTIN$^+$ cells during early postnatal DG stages. Since perinatal rNSCs were highly proliferative (50.53%; Fig EV1B), we instead estimated the recombination efficiency by assessing the number of proliferating GFP$^+$ cells out of all proliferating cells expressing the cell cycle marker KI67 (Fig EV1C). Using this approach, we observed that recombination occurred in 63.21% of all proliferating cells, in line with previously observed recombination efficiencies in (adult) NESTIN$^+$ rNSCs (Lagace *et al*, 2007). To identify astrocytes, we performed immunohistochemical stainings against glial fibrillary acidic protein (GFAP), the calcium-binding protein S100β and Acyl-CoA synthetase bubble gum family member 1 (ACSBG1), a marker for gray matter astrocytes in the developing brain (Li *et al*, 2012; Takeuchi *et al*, 2020). At P14 and P27, we observed an almost complete overlap between ACSBG1 and GFAP expression in the DG, confirming the specificity of ACSBG1 as an astrocytic marker also in the DG (Fig EV1D). To corroborate that astrocytes derive from NESTIN$^+$ rNSCs, we

searched for recombined cells, which downregulated NESTIN, but expressed astrocyte-specific marker. Indeed, we identified cells that co-expressed GFP and ACSBG1, GFAP, or S100β, indicating that NESTIN$^+$ rNSCs give rise to astrocytes in the postnatal DG (Fig 1C). Of note, early postnatal astrocytes predominantly expressed ACSBG1, while GFAP and S100β expression was initiated later (Fig 1C). To investigate the timing of rNSC-derived astrogenesis, the total numbers of ACSBG1$^+$/GFP$^+$ cells were assessed at the specific timepoints (Fig 1D and E). In the first postnatal week, we observed only few ACSBG1$^+$ astrocytes, some of which co-expressed the GFP reporter. The number of GFP$^+$ astrocytes drastically increased at P10 and P14, revealing that rNSC-mediated astrogenesis mainly occurred in the second postnatal week (Fig 1D and E; Table EV1). We corroborated our findings using another astrocyte marker, the enzyme Aldehyde Dehydrogenase 1 Family Member L1 (ALDH1L1; Fig EV1E). In the adult DG, we observed that distinct astrocyte subtypes populate different DG layers (ML, GZ, and hilus), where they exhibit a compartment-specific morphology (Beckervordersandforth *et al*, 2014). Furthermore, it has been reported that the developing DG is formed in an outside-in layering pattern (Mathews *et al*, 2010), in which embryonically derived cells contribute preferentially to the outer granule cell layer, while neurons born postnatally remain closer to the hilus (Angevine, 1965; Schlessinger *et al*, 1975; Bayer, 1980; Crespo *et al*, 1986). Thus, we next analyzed the time course of astrogenesis in distinct DG layers and observed that the ML was populated by large numbers of astrocytes already at P10, whereas in the GZ and hilus astrocytes appeared only in the subsequent days (Fig 1F; Table EV1). Hence, our data demonstrate that, in analogy to what has been reported for DG neurons (Mathews *et al*, 2010), rNSCs also generate astrocytes in an outside-in-pattern.

We next asked the question if astrocytes in the developing DG exclusively arise from rNSCs (Brunne *et al*, 2010, 2013) or whether also non-stem cell astrocytes contribute to astrogenesis in the DG. Co-staining of ACSBG1 in combination with proliferation markers (P3/P7: KI67; P10/P14: MCM2) revealed that the developing DG harboured locally proliferating astrocytes, which did not express the rNSC marker NESTIN (Fig 1G and H). Those numbers strongly increased in the second postnatal week (Fig 1I; Table EV1), as also confirmed by cell cycle marker expression in combination with ALDH1L1 (Fig EV1F). Hence, local astrocytic proliferation strongly contributed to astrogenesis, corroborating findings from neocortical development (Ge *et al*, 2012). In line with the timing of layer-specific generation of astrocytes (Fig 1F), we observed a strong increase in local astrocytic proliferation first in the ML (P10), while hilus and GZ astrocytes showed the highest proliferation rate at P14 (Fig 1J; Table EV1). To investigate a potential lineage relationship between rNSCs and proliferating astrocytes, we assessed whether rNSC-derived astrocytes (GFP$^+$/ACSBG1$^+$) co-expressed cell cycle markers. Importantly, many proliferating astrocytes expressed the GFP reporter (Fig 1K), indicating that they were indeed rNSC-derived. Together, our data support a lineage hierarchy with a perinatal rNSC at the apex giving rise to locally proliferating astrocytes that successively fill up distinct astrocytic compartments in the second week of postnatal DG development.

The developing murine DG—a special niche for simultaneous astro- and neurogenesis

There is conflicting evidence whether or not neurogenesis and astrogenesis in the developing DG occur as temporally segregated processes (Bayer & Altman, 1974; Rickmann *et al*, 1987; Brunne *et al*, 2010, 2013; Nicola *et al*, 2015) or appear simultaneously (Bond *et al*, 2020). To resolve this debate, we directly correlated timing and ratio between proliferation and generation of rNSCs, neurons, and astrocytes in the developing DG. We first conducted a retrospective analysis, as recently published by Bond *et al* (2020). Therefore, birth-dating experiments were performed, in which the thymidine analogue bromodeoxyuridine (BrdU) was injected into *Nestin*-CreER^{T2}; GFP mice at either P3, P7, P14, or P21 (Fig 2A). At the end of postnatal development (P28), the number and identity of BrdU-incorporated cells were determined, based on morphological features and the expression of cell type-specific markers (Fig 2A and B). rNSCs were identified by the expression of NESTIN and their characteristic morphology: the cell bodies of rNSCs are located in the SGZ and extend a radial process across the GZ. BrdU-incorporating astrocytes in the hilus, GZ, and ML were identified by the lack of a radial process and expression of GFAP (Fig 2B). The vast majority of BrdU$^+$ cells expressed NEUN, a marker for granule

Figure 1. Astrogenesis in the postnatal dentate gyrus (DG).

A Scheme illustrates developmental fate-mapping experiment using *Nestin*CreER^{T2}; CAG CAT GFP (from now on referred to as *Nestin*CreER^{T2}; GFP) mice to monitor radial glia-like neural stem cells (rNSCs) and their generated progeny.

B Experimental scheme of tamoxifen injection paradigm: perinatal mice were injected twice (12 h apart) to label early perinatal rNSCs and killed at postnatal day (P) 3, 7, 10, or 14 to analyze the rNSC-generated progeny within the DG layers hilus, granular zone (GZ), and molecular layer (ML).

C Confocal images of rNSC-derived astrocytes expressing GFP (green) and astrocyte-specific markers (ACSBG1, GFAP, and S100β; magenta) at different timepoints (P7, P10, and P14); lower pictures depict single-channel images the astrocyte markers (gray) used above.

D Representative pictures of recombined astrocytes (GFP$^+$/ACSBG1$^+$; arrowheads) during DG development (P3, P7, P10, and P14).

E, F Quantification of total numbers of recombined astrocytes (GFP$^+$/ACSBG1$^+$) per area at postnatal timepoints in the total DG (E) or in distinct DG compartments (F), that is, hilus, GZ, and ML indicated by different colors.

G Representative images of proliferating astrocytes (ACSBG1$^+$, cyan; arrowheads) in combination with cell cycle markers KI67 or MCM2 (magenta; P3, P7: KI67; P10, P14: MCM2).

H Confocal image of proliferating astrocytes at P10 (ACSBG1$^+$, cyan; MCM2$^+$, magenta) that did not express NESTIN (white).

I, J Quantification of total proliferating astrocytes (ACSBG1$^+$/KI67$^+$ for P3/P7; ACSBG1$^+$/MCM2$^+$ for P10/P14) per area at distinct timepoints per total DG (I) or hilus, GZ and ML (J).

K Confocal images of proliferating rNSC-derived astrocytes (GFP$^+$/ACSBG1$^+$/MCM2$^+$; arrowheads) at P10.

Data information: All data are represented as mean ± SEM; number of experimental animals throughout figure: $n = 5$ (P3) and $n = 6$ (P7, P10, P14), (E, I) indicated by red dots; all values are indicated in Table EV1; dotted lines mark GZ borders; scale bars (C, H, K) = 10 μm, (D, G) = 50 μm.
Source data are available online for this figure.

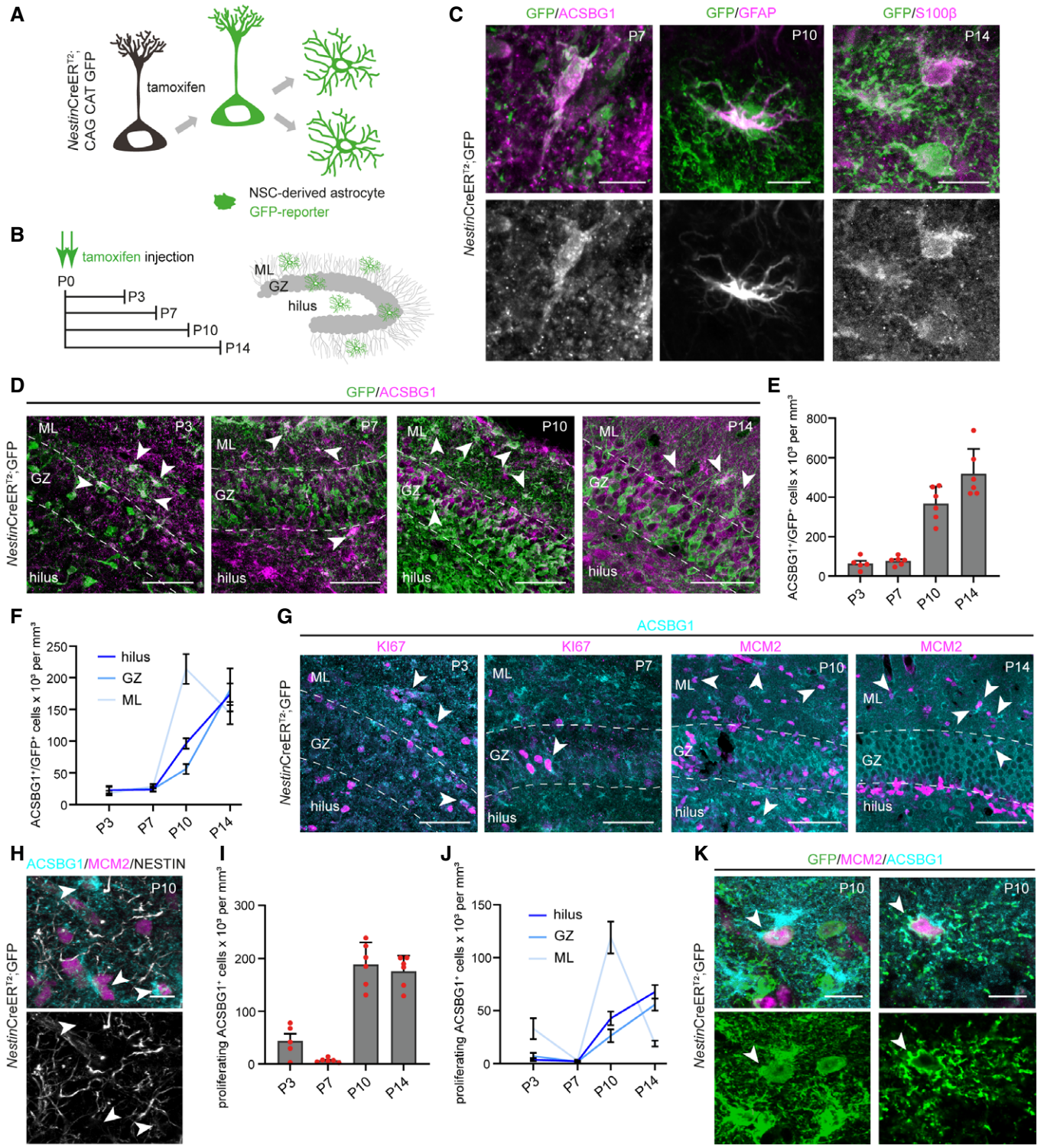

Figure 1.

neurons (Fig EV1G). Our analysis revealed that rNSCs increasingly incorporated BrdU until P14, which sharply dropped at P21 (Fig 2C; Table EV2). This is in line with findings reporting an increase in rNSC quiescence after postnatal development (Berg *et al*, 2019). In accordance with Bond *et al*., we observed both an increase in BrdU$^+$ astrocytes and neurons, strongly arguing for a simultaneous occurrence of neurogenesis and astrogenesis during postnatal DG development [Fig 2C; Table EV2; (Bond *et al*, 2020)]. However, while postnatal neurogenesis steadily increased until P14, with a subsequent drop at P21 (Fig 2C; Table EV2), astrogenesis increased until

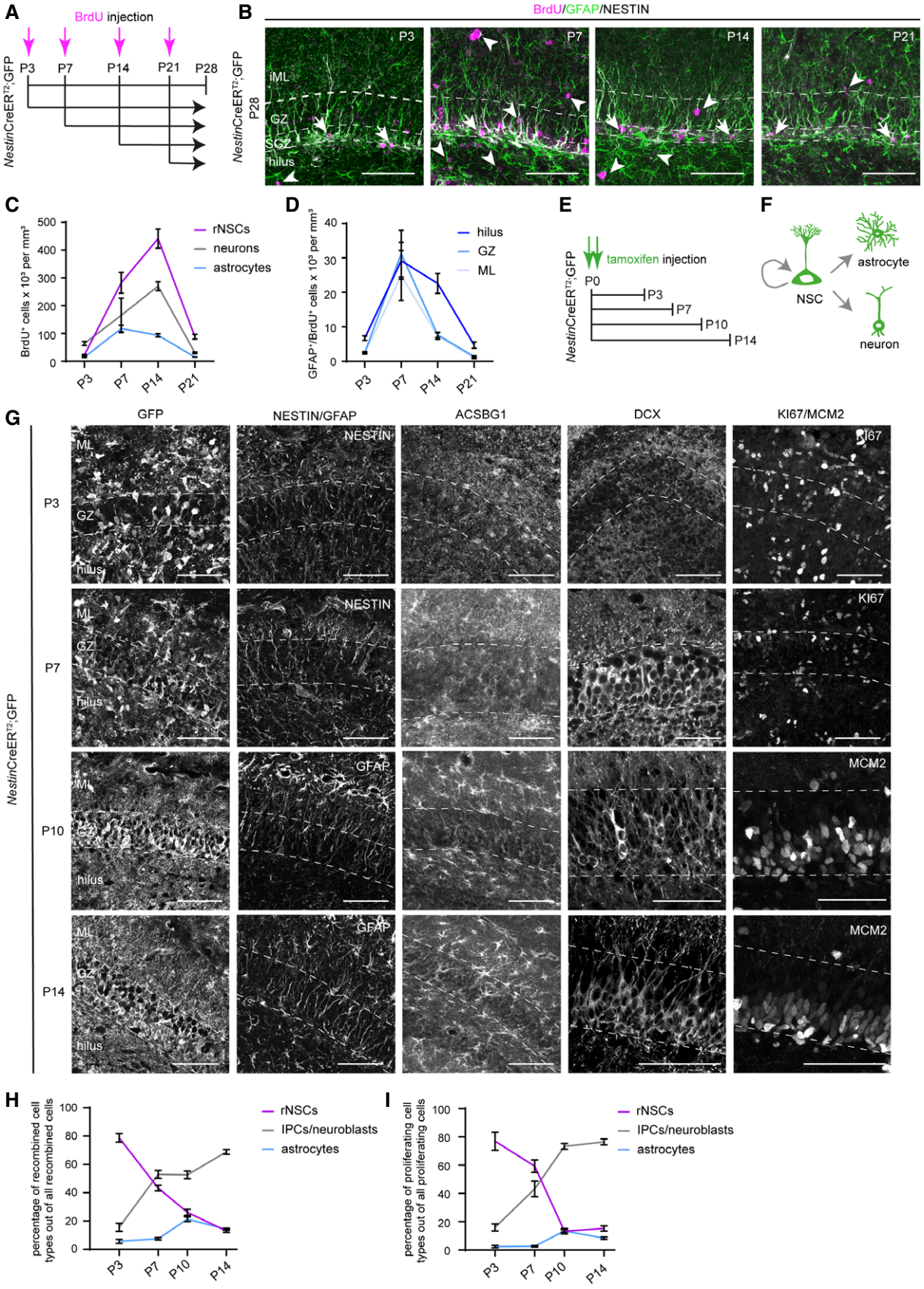
A
BrdU injection
P3
P7
P14
P21
P28
NestinCreER^T2;GFP
B
BrdU/GFAP/NESTIN
P3
P7
P14
P21
iML
GZ
SGZ
hilus
NestinCreER^T2;GFP
P28
C
BrdU+ cells x 10³ per mm³
rNSCs
neurons
astrocytes
D
GFAP+/BrdU+ cells x 10³ per mm³
hilus
GZ
ML
E
tamoxifen injection
NestinCreER^T2;GFP
P0
P3
P7
P10
P14
F
astrocyte
NSC
neuron
G
GFP
NESTIN/GFAP
ACSBG1
DCX
KI67/MCM2
NESTIN
KI67
GFAP
MCM2
ML
GZ
hilus
P3
P7
P10
P14
NestinCreER^T2;GFP
H
percentage of recombined cell types out of all recombined cells
rNSCs
IPCs/neuroblasts
astrocytes
I
percentage of proliferating cell types out of all proliferating cells
rNSCs
IPCs/neuroblasts
astrocytes

Figure 2. Simultaneous occurrence of astrogenesis and neurogenesis in the developing DG.

A Experimental scheme of birth-dating paradigm used in B-D. *Nestin*CreER^{T2}; GFP mice were injected with the thymidine analog 5-bromo-2-desoxyuridine (BrdU, pink arrows) once at distinct postnatal timepoints of DG development (P3, P7, P14, and P21) and killed at P28.

B Representative pictures of P28 animals that received BrdU at P3, P7, P14, or P21. For cell type identification of generated progeny, immunostainings against NESTIN (white), GFAP (green), and BrdU (magenta) were performed. rNSCs were identified as NESTIN$^+$/GFAP$^+$/BrdU$^+$ with a radial process (as indicated with arrows), neurons as NESTIN$^-$/GFAP$^-$/BrdU$^+$ cells, and astrocytes as NESTIN$^-$/GFAP$^+$/BrdU$^+$ cells in the hilus, GZ, and ML (arrowheads).

C Quantification of total numbers of generated cell types (rNSCs, neurons, and astrocytes) per area at distinct timepoints as indicated by different colors.

D Quantification of total numbers of newly generated astrocytes in the hilus, GZ, and ML at P3, P7, P14, and P21.

E Experimental scheme of fate-mapping paradigm used in E-H. Perinatal *Nestin*CreER^{T2}; GFP mice were injected with tamoxifen (twice, 12 h apart) and killed at P3, P7, P10, or P14.

F Scheme illustrating that recombined *Nestin*$^+$ rNSCs can self-renew and give rise to neurons and/or astrocytes.

G Representative pictures of immunostainings against cell type-specific proteins (all depicted in white). Recombined cells were identified by GFP, rNSCs by their radial process labeled with NESTIN (P3, P7) or GFAP (P10, P14), astrocytes by ACSBG1, immature neurons expressed DCX, and proliferating cells the cell cycle markers KI67 (P3, P7) or MCM2 (P10, P14).

H Quantification of the percentages of GFP$^+$ recombined cell types out of all recombined cells at distinct timepoints. Intermediate precursor cells (IPCs) identified by TBR2 expression (Fig EV1H) were added to DCX$^+$ neuroblasts.

I Quantification of the proportions of proliferating cell types (rNSCs, IPCs/neuroblasts, astrocytes) out of all proliferating cells at P3, P7, P10, P14.

Data information: Values represented as mean ± SEM; number of experimental animals: (C, D) n = 5 (P3, P21), n = 4 (P7, P14); (H, I) n = 5 (P3), n = 6 (P7, P10, P14); all numbers are indicated in Tables EV1 and EV2; dotted lines label GZ borders; scale bars = 50 μm.
Source data are available online for this figure.

P7, followed by a plateau until P14, and a decrease at P21 (Fig 2C; Table EV2). Confirming our fate-mapping results, retrospective BrdU tracing also revealed layer-specific differences in the generation of astrocytes. Astrocytes in the hilus exhibited a prolonged generation until P14 compared with upper DG layer astrocytes (GZ, ML), which peak at P7 (Fig 2D; Table EV2). At P21, astrocytes within all analyzed DG layers showed a strong decrease in BrdU incorporation (Fig 2C; Table EV2), indicating that most astrocytes have been formed by the third week of postnatal development. A limitation of the retrospective analysis is that BrdU is diluted after 2–4 cell divisions (Hughes *et al*, 1958; Dayer *et al*, 2003), indicating that we potentially underestimate the number of generated cells since the timepoint of BrdU injection. Therefore, we corroborated our results on the generation of the rNSCs, neurons, and astrocytes at specific timepoints by fate-mapping experiments using *Nestin*-CreER^{T2}; GFP mice, which received tamoxifen at P0. Zooming in on the important developmental stages P3, P7, P10, and P14, the number of rNSCs and their newly generated progeny were analyzed by morphology and cell type-specific markers (Fig 2E and F). Recombined rNSCs expressed NESTIN (P3/P7) and GFAP (P10/P14), while recombined astrocytes were identified by the lack of a radial process and expression of ACSBG1 (Fig 2G). Recombined non-glial cells were mainly positive for neuronal markers TBR2 or DCX, representing intermediate progenitor cells (IPCs) and neuroblasts, respectively (Figs 2G and EV1H). At P3, the vast majority of recombined cells were rNSCs, steadily decreasing over time, while the percentage of neurons among recombined cells strongly increased until it reached almost 70% at P14 (Fig 2H; Table EV1). In contrast, only few astrocytes were generated at early postnatal stages, peaked at P10, and evened out at P14 to 14% (Fig 2H; Table EV1). To specifically compare the ratio of proliferating rNSCs, astrocytes, and neuronal precursors out of all proliferating cells, we analyzed cell type-specific marker as described above together with proliferation marker at each postnatal timepoint (P3/P7: KI67; P10/P14: MCM2; Fig 2G). At early stages of DG development, the majority of proliferating cells were rNSCs, which substantially decreased over time (Fig 2I; Table EV1). At P10, we identified a transition from rNSC proliferation to fate-determined progenitor proliferation, which ensured the cell type-specific amplification of both neuronal and astrocytic lineages (Fig 2I, Table EV1). Neuronal precursors initially started to proliferate in the first postnatal week, followed by the astrocytic divisions, which peaked in the second postnatal week (Fig 2I, Table EV1). Our results demonstrate a simultaneous generation of neurons and astrocytes in the developing DG, which is initially accomplished through the proliferation of rNSCs giving rise to both lineages. While rNSC proliferation drops after the first week, in the second postnatal week the amplification of neuronal and astrocytic cell numbers is increasingly mediated by lineage-restricted neuronal precursor and local astrocyte proliferation. Notably, neurogenesis outweighs astrogenesis at all stages during postnatal development, leading to the characteristic overrepresentation of neurons compared with astrocytes in the adult DG.

Astrogenesis persists until adulthood

During adult life, the neuronal compartment in the DG is progressively augmented by adult rNSCs giving rise to newborn neurons. Even though the generation of new astrocytes from adult rNSCs has been first observed many years ago (Seri *et al*, 2001; Bonaguidi *et al*, 2011; Encinas *et al*, 2011), neither the mode of astrogenesis nor the number of newborn astrocytes have ever been closely examined. Here, we set out to investigate the dimension of astrogenesis and astrocytic lineage progression in the adult DG. First, we compared the quantity of astrocytes generated in the adult DG to the number of newborn neurons by performing BrdU birth-dating. Based on the results of a previous study showing that the maximum amount of BrdU-incorporated astrocytes was reached after 10 days (Encinas *et al*, 2011), BrdU was administered via drinking water for 12 days to young adult *hGFAPe*GFP mice [8-week-old; Fig 3A; (Nolte *et al*, 2001)]. Astrocytes were identified by the expression of GFP, GFAP and sex-determining region Y-box 2 (SOX2). SOX2 is expressed in the vast majority of GFAP$^+$ astrocytes in the hilus and GZ (93.2 and 98.4%, respectively; Fig EV2A and B) and strongly overlapped with ACSBG1 expression in the adult DG (Fig EV2C). However, rNSCs and IPCs in the SGZ also express SOX2. SOX2$^+$/GFAP$^+$ rNSCs were specifically identified by their radial glial

process, IPCs and neuroblasts by the expression of SOX2 and DCX, respectively (Fig 3B). After assessing the identity and number of BrdU-incorporated cells (Fig EV2D and E; Table EV3), we calculated the ratio of rNSCs, newly generated IPCs/neuroblasts, and astrocytes. This analysis revealed that very few rNSCs incorporated BrdU, while the vast majority of BrdU$^+$ cells were IPCs/neuroblasts (1 and 91%, respectively; Fig 3C; Table EV3). Nevertheless, a substantial number of astrocytes could be identified among these newly generated cells (7%; Fig 3C; Table EV3). Like done for our analysis during DG development, we investigated the frequency of astrocytes associated with distinct DG compartments within the group of BrdU-incorporating astrocytes. Astrocytes within the hilus made up the majority with 54%, followed by ML astrocytes (32.1%), and GZ astrocytes (13.9%), confirming that newly generated astrocytes are populating all DG layers in adulthood (Fig 3D and E; Table EV4). The vast majority of newly generated and proliferating cells in the SGZ belonged to the neuronal lineage. Hence, astrogenesis was only quantified within the hilus, GZ and ML of the adult DG.

Next, we wanted to assess where newborn astrocytes originate from. Interestingly, and analogous to DG development, we observed astrocytes expressing the cell cycle marker MCM2 (Figs 3F and EV2F). While proliferating astrocytes were detected in all DG layers, they appeared at a different rate (Figs 3F and G, and EV2F). Hilus astrocytes constituted 61.1% of all proliferating astrocytes, while GZ and ML astrocytes proliferated less (Fig 3G; Table EV4). Dividing GFP$^+$/GFAP$^+$/SOX2$^+$ astrocytes substantially downregulated GFAP protein in many MCM2$^+$ cells, while the expression of *hGFAP*eGFP and SOX2 was unaltered (Figs 3H and EV2G). Interestingly, the proliferation rate of astrocytes across DG layers (Fig 3G; Table EV4) matched very well with the rate of newly generated astrocytes within different DG compartments (Fig 3E, Table EV4), suggesting that the majority of newly generated astrocytes potentially derive from locally dividing astrocytes.

To assess to which extent adult astrogenesis is mediated by rNSCs (Fig 3I), we performed fate-mapping experiments using *Nestin*CreER^{T2}; GFP mice (Fig 3I and J). Recombination in rNSCs was induced by 5 days of tamoxifen administration (10×; every 12 h) in 8-week-old mice (Fig 3J). Twelve days post-induction, we observed that the majority of recombined cells (indicated by the GFP reporter) differentiated into DCX$^+$ neuronal cells (62.97%; IPCs and neuroblasts), and a high number of GFP$^+$ cells still retained rNSC identity (32.23%; Figs 3K and L, and EV2H; Table EV3). We rarely observed rNSC-derived astrocytes, contributing to only 0.55% of the total recombined cells (Figs 3K and L, and EV2H; Table EV3). Among those, the vast majority were located in the hilus (93.46% of all recombined astrocytes), few in the GZ (6.54% of all recombined astrocytes), and none in the ML (Fig 3M; Table EV4). Notably, we found few examples of GFP$^+$ astrocytes expressing the cell cycle marker MCM2 (Fig 3N) in the hilus and GZ, suggesting that rNSCs in the adult DG can give rise to astrocytes which can further

Figure 3. Astrogenesis persists until adult stages of the DG.

A Experimental scheme of adult BrdU birth-dating paradigm used in B-E. Adult mice were administered with BrdU via drinking water for 12 consecutive days. For all experiments shown in B-H, adult *hGFAP*eGFP mice were used.

B Confocal image of an adult DG populated by distinct cells identified by cell type-specific protein expression and morphology. All cells newly generated within the 12 days incorporated BrdU (magenta); rNSCs were identified by expression of SOX2 (cyan), localization of their cell bodies to the SGZ, and a GFAP$^+$ radial process (green); IPCs were located within the SGZ and express SOX2 only (cyan); neuroblasts in the SGZ and GZ were labeled by DCX (white; arrows); astrocytes in the hilus, GZ, and ML (arrowheads) expressed SOX2 (cyan). Single channel images are depicted in Fig EV2E.

C Quantification of the percentages of generated cell types out of all generated cells (rNSCs, IPCs + neuroblasts, astrocytes) in the DG. Total numbers of all generated cells within 12 days are depicted in Fig EV2D.

D Representative picture of astrocytes located to distinct DG layers (hilus, GZ, and ML). Co-expression of BrdU/SOX2/GFAP revealed that all DG compartments harboured astrocytes, which were newly generated during adulthood (arrowheads).

E Quantification of the proportions of generated astrocytes per DG layer out of all generated DG astrocytes.

F Representative image of proliferating astrocytes (SOX2$^+$/MCM2$^+$; cyan and magenta, respectively; arrowheads) of all DG layers. Singe channel images are depicted in Fig EV2F.

G Quantification of the percentages of proliferating astrocytes in distinct DG layers over all proliferating DG astrocytes.

H Confocal images showing GFP$^+$/GFAP$^+$/SOX2$^+$ astrocytes of distinct DG layers co-expressing the proliferation marker MCM2 (white; single channels are represented in Fig EV2G).

I Scheme illustrating adult fate-mapping experiment using *Nestin*CreER^{T2}; GFP mice to monitor rNSCs and their generated astrocytic progeny. Two potential modes of adult astrogenesis and their lineage relation are depicted: (1) rNSC-derived astrogenesis and (2) astrocyte-derived astrogenesis.

J Tamoxifen induction protocol used in (K–N). Adult *Nestin*CreER^{T2}; GFP mice were intraperitoneally injected with tamoxifen for 10 times at 5 consecutive days (12 h apart) and killed 12 dpi.

K Representative image of recombined cells (GFP$^+$, green) of different cellular identity: rNSCs [SOX2$^+$ (cyan) with a NESTIN$^+$ radial process (white)], IPCs (SOX2$^+$ nuclei in the SGZ; cyan), DCX$^+$ neuroblasts in the SGZ and GZ (magenta), and astrocytes (SOX2$^+$ cells in the hilus, GZ, and ML; cyan). Single channel images are represented in Fig EV2H.

L Quantification of the proportions of recombined cell types over all recombined DG cells (rNSCs, IPCs + neuroblasts, astrocytes).

M Quantification of the percentages of rNSC-derived astrocytes in distinct DG layers over all recombined DG astrocytes.

N Confocal images of proliferating rNSC-derived astrocytes (GFP$^+$/SOX2$^+$/MCM2$^+$; arrowheads) in hilus and GZ.

O Experimental timeline of *in vivo* two-photon imaging *hGFAP*-RFP. AAV2/9-hsyn-jGCaMP7 virus served to provide neuronal landmarks and was injected immediately before the implantation of the hippocampal imaging window. Repetitive imaging was performed 28-day post-injection/implantation.

P Scheme of hippocampal imaging window facilitating optical access to the DG and even hilus.

Q Representative examples of field views captured within the hippocampal fissure (indicated by the abundant large vessels), the GZ with its densely packed granule neurons and the hilus containing much larger neuronal somata; expression of GCaMP7 virus (green), labeling of astrocytes by *hGFAP*-RFP (red).

R Examples of locally dividing astrocytes (arrows) derived from two experimental animals. Arrowheads depict landmarks that served for identification.

Data information: All data are represented as mean ± SEM; number of experimental animals (indicated by red dots): (C, E) $n = 5$, (G) $n = 4$, and (L, M) $n = 3$; numbers are indicated in Tables EV3 and EV4; dotted lines border SGZ and GZ; scale bars = 10 μm (H, N), and 50 μm (B, D, F, K, Q, R). dpi, days post-injection.
Source data are available online for this figure.

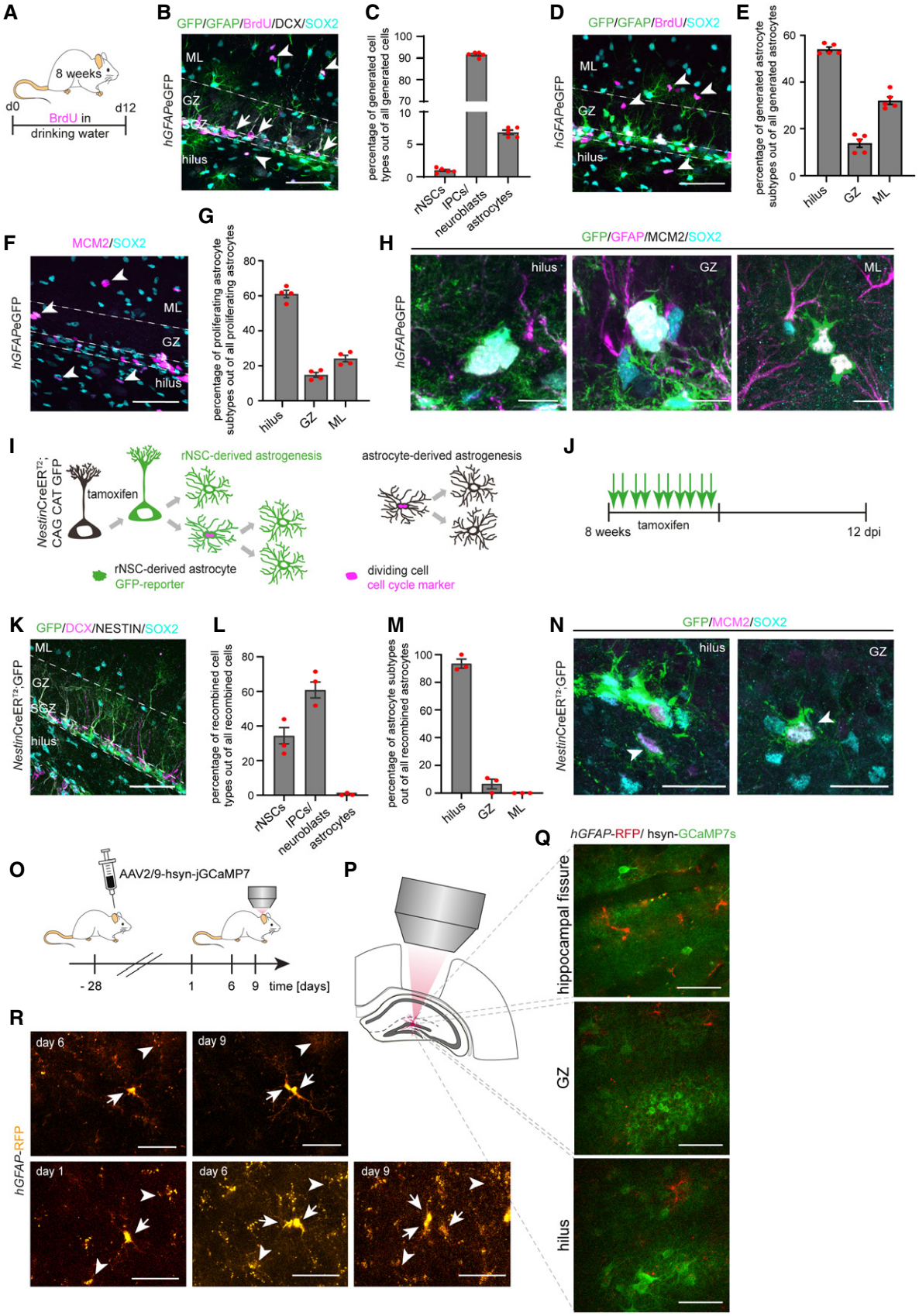

Figure 3.

proliferate. Overall, our data indicate a similar lineage relation as described for postnatal DG development, in which rNSCs generate astrocytes with proliferative capacity that contribute to astrogenesis by local proliferation. However, rNSC-mediated astrogenesis is a rare event in the adult DG and the vast majority of newborn astrocytes are generated by locally dividing astrocytes. Of note, both generation and proliferation of adult astrocytes were confirmed using an additional mouse line (*Nestin*CreER^{T2}; YFP, Fig EV2I–L; Tables EV3 and EV4).

Given their role as major driver of adult astrogenesis, the next question was how often local astrocytes can proliferate in the adult neurogenic niches. To assess this, we first performed *in vitro* live imaging of subependymal zone (SEZ) cultures. NSCs from the SEZ of *hGFAP*-RFP animals were isolated, and time-lapse video microscopy was performed for one week under differentiating conditions. Cell division and lineage progression of individual NSCs were tracked by lineage tree analysis (Costa *et al*, 2011), and only clones containing astrocytes were further analyzed. These experiments elucidated that astrocytes derived through asymmetric NSC division and were able to divide 1–2 times to produce 2–3 astrocytes (Fig EV3A; Movie EV1). To corroborate our findings *in vivo*, we next performed intravital two-photon imaging in the adult hippocampus (Fig 3O). To visualize astrocytes, we implanted a hippocampal window in adult *hGFAP*-RFP mice. During the window surgery, we injected AAV2/9-hsyn-jGCaMP7s to facilitate the expression of the genetically encoded calcium indicator GCaMP7s to serve as anatomical references during *in vivo* imaging (Fig 3O). After a 4-week waiting period, we repetitively scanned the same region of the dorsal hippocampus spanning the CA1 area up to the DG (up to 750 µm in z; Fig 3O–Q). In agreement with our observation from *in vitro* imaging, we found that astrocytes in the adult hippocampus nearby the fissure were able to generate 2–3 astrocytes by 1–2 local proliferations (Fig 3R; $n = 2$ animals). Together, our results show that hippocampal astrogenesis persists into adulthood where it is predominantly driven by local astrocytes proliferation.

Adult astrogenesis is a dynamic and inducible process

Adult neurogenesis is not a fixed process but permits cellular and molecular remodeling in response to environmental stimuli. Voluntary physical activity is the most potent known stimulus to enhance adult neurogenesis in the DG, which is mediated by a robust increase in neural stem and progenitor cells proliferation, leading to improved cognitive abilities and mood in animals and in humans (van Praag *et al*, 2005; van Praag, 2008). Aging on the contrary is regarded as a major negative regulator of adult neurogenesis due to a decrease in progenitor numbers and proliferation capacity, as well as impaired differentiation and survival of newborn neurons (Kuhn *et al*, 1996; Ben Abdallah *et al*, 2010; Walter *et al*, 2011; Lee *et al*, 2012; Harris *et al*, 2021). We thus asked if adult astrogenesis is also affected by pro- and anti-neurogenic stimuli (voluntary exercise and aging, respectively) by assessing the number of newly generated and proliferating astrocytes upon voluntary exercise and during aging. For the voluntary exercise paradigm, 8-week-old *hGFAP*eGFP mice got deliberate access to running wheels for 12 days and the distance traveled was monitored. Littermates without access to running wheels served as controls (Fig 4A). To label newly generated cells, BrdU was administered through drinking water over those 12 days and generated rNSCs, IPCs, and neuroblasts, and astrocytes in the hilus, GZ, and ML of control and running animals were analyzed (Fig 4A and B). In accordance with previous reports (van Praag *et al*, 1999a, 1999b; Farioli-Vecchioli *et al*, 2014), access to running wheels significantly increased the number of BrdU-incorporated rNSCs, IPCs, and neuroblasts (Fig 4C, Table EV3). Intriguingly, we also observed a significant increase in the number of BrdU$^+$ astrocytes, indicating that—like adult neurogenesis—adult astrogenesis can be stimulated. Again, we confirmed these observations in an additional mouse line (*Nestin*CreER^{T2}; YFP; Fig EV3B and C; Table EV3). Interestingly, the percentages of newly generated neurons and astrocytes out of all newborn cells did not change between control and exercise conditions (Fig 4D; Table EV3). The

Figure 4. Dynamics of adult astrogenesis under pro-neurogenic conditions.

A Experimental scheme of pro-neurogenic BrdU birth-dating paradigm used in B-D. 8-week-old *hGFAP*eGFP mice had access to running wheels, controls were housed under standard conditions. All mice were administered with BrdU via drinking water for 12 days and BrdU- incorporation was analyzed at day 12.

B Representative images of BrdU-incorporating newly generated cells in control and running *hGFAP*eGFP animals. BrdU$^+$ cells (magenta) were assigned to distinct cell types: rNSCs [identified by their SOX2$^+$ (cyan) cell bodies residing in the SGZ with a GFAP$^+$ radial process (green)]; IPCs/neuroblasts [SOX2$^+$ (cyan) nuclei located to the SGZ, DCX$^+$ cells (white) in the SGZ and GZ, respectively], and astrocytes [SOX2$^+$ cells (cyan) in the hilus, GZ, and ML]. Arrows mark newly generated neuronally committed cells (BrdU$^+$/DCX$^+$), while arrowheads indicate BrdU$^+$ astrocytes (SOX2$^+$).

C Quantification of total numbers of generated cell types (BrdU$^+$) per area in the DGs of control and runner animals. rNSCs: ****$P < 0.0001$; IPCs/neuroblasts: ***$P = 0.0007$; astrocytes: **$P = 0.0032$; unpaired *t*-test.

D Quantification of the percentages of generated cell types out of all generated cells (rNSCs, IPCs + neuroblasts, astrocytes) in the DGs of controls and runners; not significant, unpaired *t*-test.

E Representative images of proliferating (MCM2$^+$; magenta) cells of adult control and running *hGFAP*eGFP animals; rNSCs, IPCs (arrows) and astrocytes (arrowheads) were identified by criteria described in (B). Single channel images are represented in Fig EV3D.

F Quantification of total numbers of proliferating cell types (MCM2$^+$) per area in the DG of controls and runners. rNSCs: **$P = 0.0052$; IPCs: ***$P = 0.0008$; astrocytes: *$P = 0.0210$; unpaired *t*-test.

G Experimental scheme of pro-neurogenic fate-mapping paradigm used in (H, I). 8-week-old *Nestin*CreER^{T2}; GFP mice were intraperitoneally injected with tamoxifen for five days (10 times, every 12 h). After tamoxifen induction, runners had access to running wheels, controls were housed in standard conditions for 12 days after tamoxifen injections.

H Representative images of recombined (GFP$^+$; green) cells of distinct cellular identities: rNSCs [SOX2$^+$ (cyan) with a NESTIN$^+$ radial process (white)], IPCs (SOX2$^+$ nuclei in the SGZ; cyan), DCX$^+$ neuroblasts in the SGZ and GZ (magenta), and astrocytes (SOX2$^+$ cells in the hilus, GZ, and ML; cyan).

I Quantification of the total numbers of recombined cell types (GFP$^+$) per area in the DG of controls and runners; rNSC: $P = 0.074$; IPCs/neuroblasts: *$P = 0.0460$; astrocytes: $P = 0.2314$; unpaired *t*-test.

Data information: All data are represented as mean ± SEM; number of experimental animals (indicated by red dots): (C,D) $n = 5$ for controls, $n = 6$ for runners; (F) $n = 4$ for controls, $n = 5$ for runners; (I) $n = 3$ for both controls and runners; numbers are depicted in Table EV3; dotted lines border SGZ and GZ; scale bars = 50 µm.
Source data are available online for this figure.

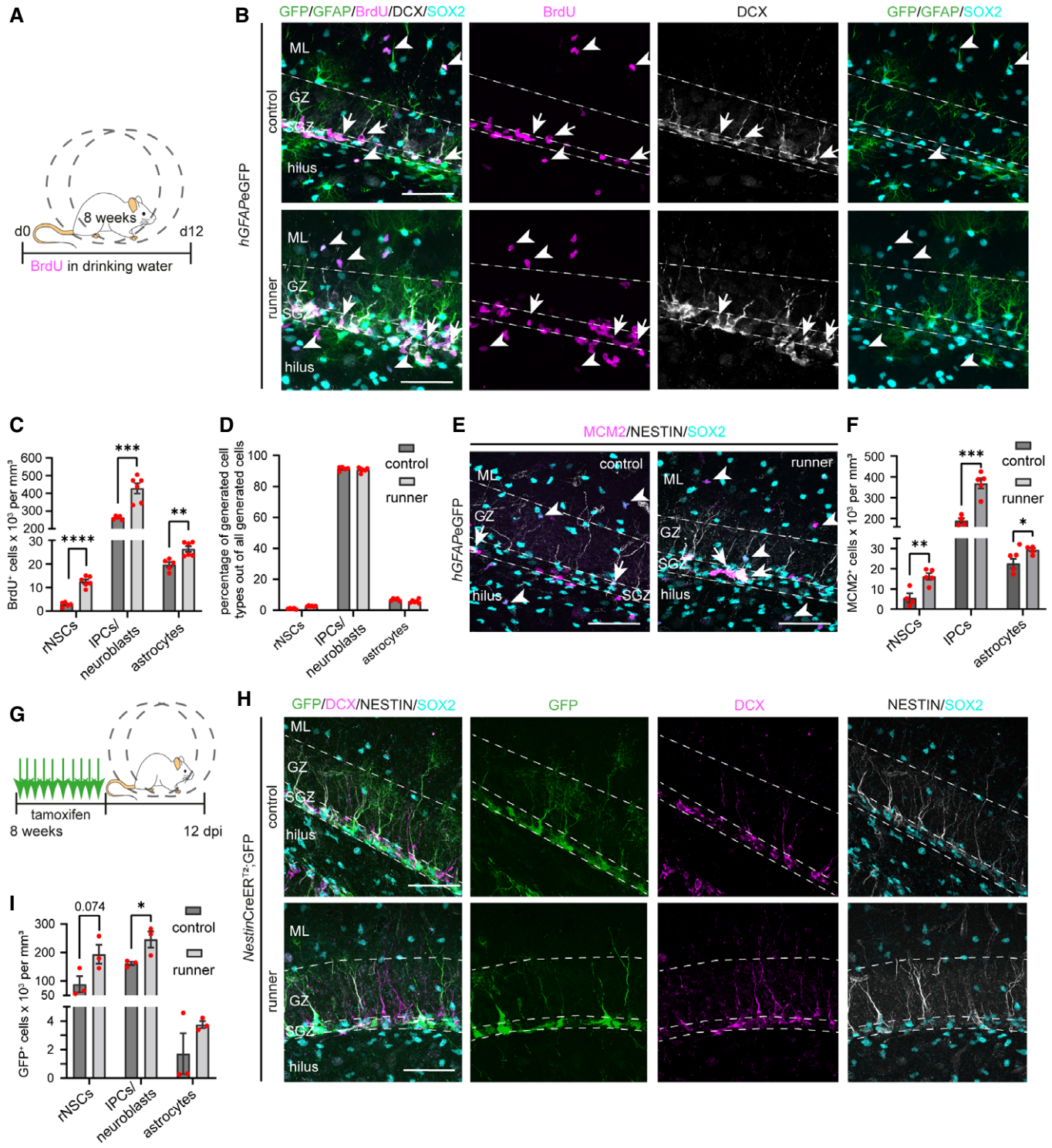

Figure 4.

adult DG is characterized by an extraordinarily high number of neurons (Bonthius *et al*, 2004; Keller *et al*, 2018) and comparatively low number of astrocytes, leading to an estimated neuron-to-astrocyte ratio of approximately 20:1. This ratio is also reflected by the proportion of neurons and astrocytes among newly generated cells with and without a pro-neurogenic stimulus (Fig 4D), suggesting that in the adult DG, neurogenesis and astrogenesis are balanced processes to maintain a stable cellular composition of the DG. Next, we unraveled the source of the additional newly generated astrocytes induced by the running wheel stimulus by assessing the number

and identity of proliferating cells (Figs 4E and EV3D; Table EV3). In accordance with published data, showing that the increase in neurogenesis upon running is a direct consequence of the enhanced proliferation of neuronal precursor cells (Kempermann *et al*, 1997; Kempermann & Gage, 2002; Overall *et al*, 2013), we observed a significant increase in rNSCs and IPCs upon running (Fig 4E and F, Table EV3). Furthermore, the number of proliferating astrocytes was significantly enhanced in the DG of running mice (Fig 4F, Table EV3), indicating that also under exercise conditions, most adult-born astrocytes derive from locally proliferating astrocytes. To further specify the origin of adult-born astrocytes in running mice, we performed fate-mapping experiments using *Nestin*CreER^{T2}; GFP mice as described above, followed by subsequent access to running wheels for 12 days (Figs 3I and J, and 4G and H). Starting from the same pool of recombined cells, we analyzed the total number of GFP$^+$ rNSCs, IPCs/neuroblasts, and astrocytes (Fig 4H and I). In comparison with animals housed under standard conditions, the runners exhibited an increase in the total number of neuronally determined recombined cells, while the number of rNSC-derived astrocytes did not significantly change (Fig 4H and I; Table EV3). This corroborates the finding that NESTIN$^+$ neural stem and precursor cells primarily contributed to the observed running-induced increase in newborn neurons, while the increase in newly generated astrocytes was rather mediated by the proliferation of local astrocytes.

To probe the impact of anti-neurogenic conditions on astrogenesis, we carried out the same experiments in aging mice. Aging has been shown to substantially hamper adult neurogenesis already in middle-aged mice by diminishing both number and maturation of newborn neurons (Kuhn *et al*, 1996; Heine *et al*, 2004; Olariu *et al*, 2007) and depleting the rNSC pool by cell death, terminal differentiation, and increased quiescence (Kempermann *et al*, 1998; Bondolfi *et al*, 2004; van Praag *et al*, 2005; Ben Abdallah *et al*, 2010; Encinas *et al*, 2011; Harris *et al*, 2021). Astrocytes in aged animals display a greater immunoreactivity of GFAP and longer and thicker processes, almost resembling reactive astrocytes (Shetty *et al*, 2005; Bondi *et al*, 2021). Besides terminal differentiation of rNSCs into astrocytes (Encinas *et al*, 2011), nothing is known about how astrogenesis is affected in the aged DG. Using the above-described paradigms (Figs 3A and 4A), we assessed the number and identity of BrdU-incorporating cells in middle-aged (14 months) and aged (21 months) *hGFAP*eGFP animals (Fig 5A–C). Confirming previous reports, we observed a sharp drop in the total number of BrdU-incorporating rNSCs and neuroblast at 14 months of age (Fig 5C, Table EV3). These numbers did not significantly decline any further at 21 months of age (Fig 5C, Table EV3). To our surprise, the number of BrdU$^+$ astrocytes did not significantly differ between young and middle-aged animals (Fig 5C, Table EV3). Instead, we detected a significant decline in the number of newly generated astrocytes only in aged animals (Fig 5C; Table EV3). While the ratio between newborn neurons and astrocytes was balanced in young adults (both under control and exercise conditions), we now observed a shift toward an increased astrocyte generation (Figs 4D and 5D; Table EV3). However, this shift was not mediated by an increase in astrogenesis per se as the number of proliferating astrocytes was significantly decreased at 14 and 21 months of age (Fig 5E and F; Table EV3). Instead, this shift was mediated by the severe loss (20-fold decline) of proliferating neuronal precursors (Fig 5F; Table EV3). Although the number of proliferating rNSCs was reduced, they did not reach significance (Fig 5F, Table EV3). Further corroborating the cause of the observed phenotypes, we administered tamoxifen to 14-month-old *Nestin*CreER^{T2}; GFP animals and assessed the identity of recombined cells at 12-day-post-injection (dpi) according to previous experiments (Fig 4G–I). Aging led to a significantly reduced number of recombined rNSCs and to a 30-fold decline in neurogenesis (Fig 5G and H; Table EV3). At 14 months, we did not observe a single rNSC-derived astrocyte after 12 days (Fig 5H; Table EV3), an indication that newborn astrocytes during aging originate again predominantly, if not exclusively, from locally proliferating astrocytes.

Taken together, our results show that astrogenesis in the DG exists beyond early postnatal stages into adulthood. Even though rNSCs occasionally generate astrocytes, adult astrogenesis is primarily driven by local division of morphologically differentiated astrocytes. Intriguingly, as described for neurogenesis, the process of astrogenesis can adapt to environmental stimuli, suggesting an unexpected level of plasticity of the astrocytic compartment.

scRNA-sequencing analysis of astrocyte dynamics

In order to assess astrocyte dynamics on a molecular level, we carried out single-cell RNA sequencing (scRNA-seq) of DG astrocytes of *hGFAP*eGFP mice. Here, adult animals (8-week-old) held under standard conditions served as controls and were compared with littermates that had access to a running wheel for 12 days and to 14-month-old *hGFAP*eGFP animals (non-running conditions). For scRNA-seq analysis, we dissected the DGs of 4 animals of each condition (two males and two females). All DGs belonging to the same experimental group were pooled and dissociated to single cells. Around 5000 cells per condition were used for library preparation without any further separation of cell types. scRNA-seq was performed using the droplet-based 10X Genomics platform, and the quality for each sample was controlled by calculating gene counts per cell, UMI counts per cell, and percent of mitochondrial transcripts per cell using the Seurat R package (Butler *et al*, 2018). Cell clustering was conducted, and the cluster identity was determined by known marker gene expressions (Fig 6A). All expected cell types of the DG could be identified for each condition (Fig 6B). To reveal potential mechanisms underlying astrocyte dynamics observed under distinct conditions, we included only the astrocyte cluster for further analysis, which was identified by the expression of known astrocyte markers such as *Aldoc*, *Aldh1lL1*, *Sox9*, *Slc1a3*, and *Slc1a2* (Fig EV4A–F). First, we observed that clustering of astrocytes did not differ between the conditions, suggesting a common set of transcribed astrocytic genes (Fig 6C). Next, we identified differentially expressed genes comparing (i) young non-runners to young runners (Fig 6D and E) and (ii) young non-runner to aged non-runners (Fig 6F and G). Astrocyte data sets for each condition are summarized in Tables EV5–EV8, and whole scRNA-seq data sets are available at GEO (GSE190399). This analysis revealed only very few significantly differentially regulated genes (Tables EV5–EV8), indicating that overall astrocytic transcription is not significantly affected by distinct stimuli. To still be able to assess subtle transcriptomic alteration, we performed GO-term analysis of all non-significantly differentially regulated genes by a statistical overrepresentation test for biological processes using Panther

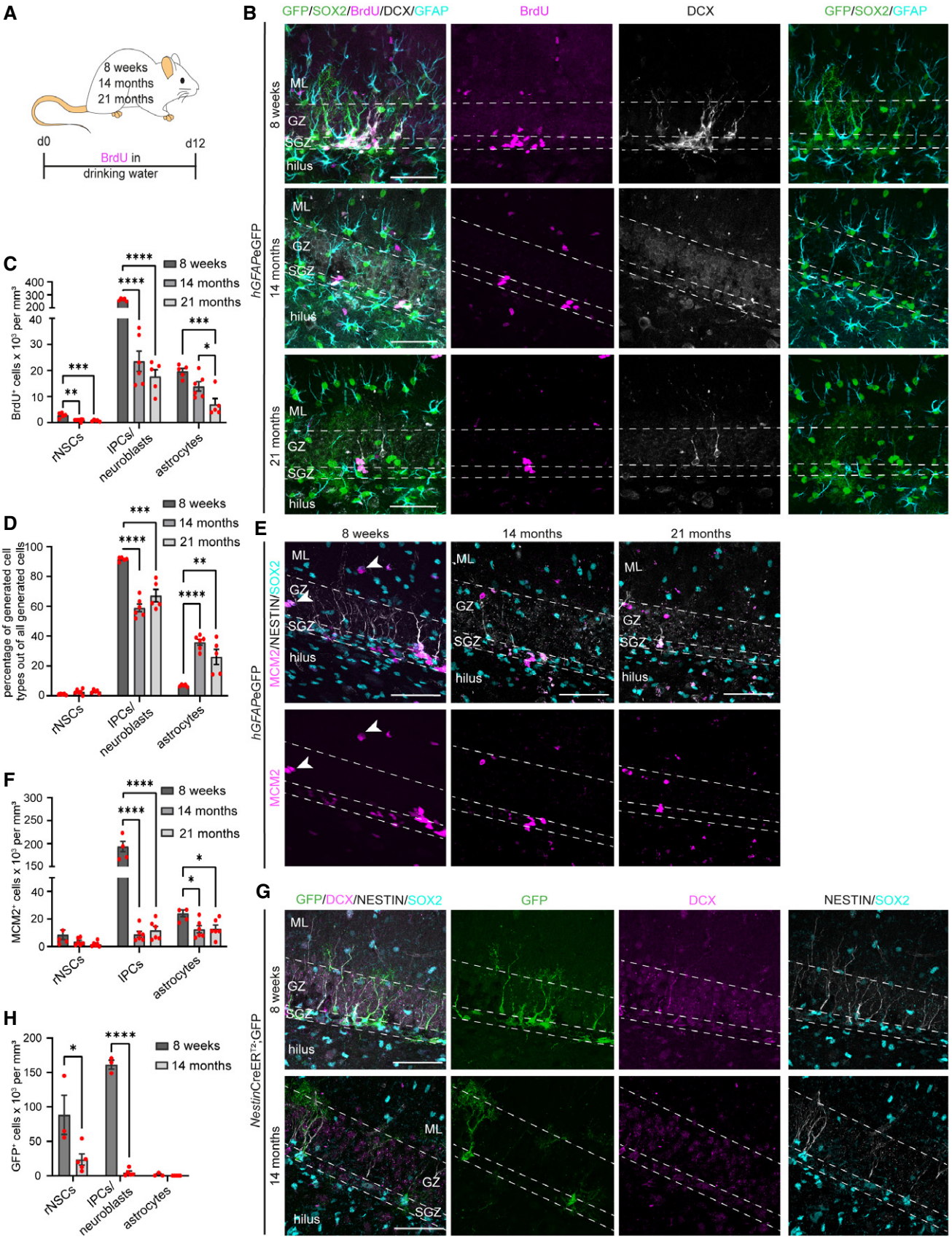

Figure 5.

Figure 5. Dynamics of adult astrogenesis under anti-neurogenic conditions.

A Experimental scheme of adult and aging BrdU birth-dating paradigm used in B-D. 8-week-, 14-month-, and 21-month-old *hGFAP*eGFP animals were administered with BrdU via drinking water for 12 days, and generated ($BrdU^+$) cells were analyzed at day 12.

B Representative confocal images of BrdU-incorporating cells (magenta) assigned to distinct cell types of 8-week-, 14-month-, and 21-month-old *hGFAP*eGFP mice: rNSCs [identified by their $SOX2^+$ (green) cell bodies residing in the SGZ with a $GFAP^+$ radial process (cyan)]; IPCs/neuroblasts [$SOX2^+$ (green) nuclei located to the SGZ, DCX^+ cells (white) in the SGZ and GZ, respectively], and astrocytes [$SOX2^+$ cells (green) in the hilus, GZ, and ML].

C Quantification of total numbers of generated cell types ($BrdU^+$; rNSCs, IPCs + neuroblasts, astrocytes) per area in the DGs of 8-week-, 14-month-, and 21-month-old *hGFAP*eGFP animals. rNSCs: ***$P = 0.00076$, **$P = 0.0014$; IPCs/neuroblasts ****$P < 0.0001$; astrocytes: ***$P = 0.0008$; *$P = 0.0403$; one-way ANOVA with Tukey's *post hoc* test.

D Quantification of the percentages of generated cell types out of all generated cells (rNSCs, IPCs + neuroblasts, astrocytes) in the DG of 8-week-, 14-month-, and 21-month-old animals. rNSCs: not significant; IPCs/neuroblasts ****$P < 0.0001$, ***$P = 0.0001$; astrocytes: **$P < 0.0019$, ****$P < 0.0001$; one-way ANOVA with Tukey's *post hoc* test.

E Representative images of proliferating cells ($MCM2^+$; magenta): rNSCs [$SOX2^+$ cell nuclei (cyan) residing in the SGZ with a $NESTIN^+$ radial process (white)]; IPCs [$SOX2^+$ nuclei (cyan) located to the SGZ], and astrocytes [$SOX2^+$ cells (cyan) in the hilus, GZ, and ML; arrowheads].

F Quantification of total numbers of proliferating ($MCM2^+$) cell types per area in the DGs of 8-week-, 14-month-, and 21-month-old animals. rNSCs: not significant; IPCs ****$P < 0.0001$; astrocytes: *$P = 0.0216$; *$P = 0.0266$; one-way ANOVA with Tukey's *post hoc* test.

G Confocal images of 8-week- and 14-month-old *Nestin*$CreER^{T2}$; GFP animals, which received tamoxifen for 5 days (10 times, every 12 h) and were killed 12 days after the last tamoxifen shot. The majority of recombined cells were rNSCs [$SOX2^+$ cell nuclei (cyan) residing in the SGZ with a $NESTIN^+$ radial process (white)] and IPCs/neuroblasts [$SOX2^+$ (cyan) nuclei located to the SGZ, DCX^+ cells (magenta) in the SGZ and GZ, respectively], and only very few astrocytes [$SOX2^+$ cells (cyan) in the hilus, GZ, and ML] were generated by initially recombined rNSCs.

H Quantification of total numbers of recombined (GFP^+) rNSCs, IPCs/neuroblasts, astrocytes per area in the DGs of 8-week- and 14-month-old animals. rNSCs: *$P = 0.0460$; IPCs/neuroblasts: ****$P < 0.0001$; astrocytes: not significant; unpaired *t*-test.

Data information: All data are represented as mean ± SEM; number of experimental animals (indicated by red dots): (C,D) $n = 5$ in 8-week-old mice, $n = 6$ in 14-month-old mice, $n = 5$ in 21-month-old mice; (F) $n = 4$ in 8-week-old mice, $n = 6$ in 14-month- and 21-month-old mice; (H) $n = 3$ in 8-week-old mice, $n = 5$ in 14-month-old mice; values are indicated in Table EV3; dotted lines border SGZ and GZ; scale bars = 50 μm.
Source data are available online for this figure.

(https://www.pantherdb.org; Appendix Tables S1 and S2). This analysis revealed the following selected GO-terms as overrepresented in astrocytes isolated from the DG of running mice in comparison with control animals: mRNA processing, RNA splicing, lysosomal transport, regulation of cell growth and others (Fig 6E). Notably, genes associated with gliogenesis, glial cell differentiation, and development, as well as glial cell migration, were statistically overrepresented among the potential upregulated genes in astrocytes from running mice, supporting our observation that astrogenesis by local astrocyte division in running conditions was significantly increased. GO-term analysis of potentially differentially downregulated genes in astrocytes from running mice revealed a strong overrepresentation of terms related to mitochondrial respiration (Fig 6E). Interestingly, the comparison between young adult and aged mice identified many statistically overrepresented GO-terms associated with synapse organization/assembly and axogenesis in DG astrocytes from aged animals alongside epithelial cell differentiation and astrocyte differentiation (Fig 6G). Given that neurogenesis is strongly decreased in 14-month-old animals, these observations indicate that one potential role of astrocytes in the aged DG may be the strengthening of neuronal connection between existing neurons and their maintenance.

Discussion

While neurogenesis and oligodendrogenesis are well characterized, both in terms of the lineage's progressive differentiation and markers for the specific stages (El Waly *et al*, 2014; Beckervordersandforth *et al*, 2015; Bond *et al*, 2015; Sock & Wegner, 2019), astrogenesis is still a highly understudied process. Two recent publications reported on adult astrogenesis in the diencephalon (Ohlig *et al*, 2021) and the cortex (Batiuk *et al*, 2020), using scRNA-seq and clonal analysis. While cortex and diencephalon are non-neurogenic regions of the adult brain, the DG features a specialized form of plasticity due to the life-long generation of new neurons and astrocytes (Suh *et al*, 2007; Bonaguidi *et al*, 2011; Encinas *et al*, 2011). Despite the important regulatory contribution of astrocytes to the process of adult neurogenesis (Song *et al*, 2002; Lie *et al*, 2005; Ehret *et al*, 2015; Schneider *et al*, 2019), very little is known about the establishment, the maintenance, and the remodeling of the astrocyte compartment in the DG. Implying a vital role of astrocytes to hippocampal function and plasticity, as well as astrocytic contribution to the pathologies of neurodegenerative and neuropsychiatric disorders, we here set out to comprehensively assess astrogenesis and astrocyte dynamics over the life span of a mouse (Fig 7A and B).

To determine the principles of astrogenesis, the first question posed was on the cellular and temporal origin of DG astrocytes. Starting at early postnatal DG development, we conducted genetic fate-mapping, proliferation analysis, and retrospective birth-dating experiments to reveal at which timepoint the first astrocytes appear and where they come from. Recombination of *Nestin*$CreER^{T2}$; GFP animals at P0 identified $Nestin^+$ rNSCs as the origin of DG astrocytes. This is supported by clonal analysis showing that highly neurogenic rNSCs expressing the transcription factor *HopX* can give rise to few astrocytes (Berg *et al*, 2019). While the first astrocytes appeared as early as P3, we observed a surge of astrogenesis from P10 to P14 (Fig 7A). The next question was how this increase in astrocyte numbers is mediated. Time-lapse imaging of *hGFAP*eGFP mice demonstrated that rNSCs contribute to astrogenesis not only by proliferation but also by terminal differentiation into astrocytes (Brunne *et al*, 2010). However, our analysis showed that rNSCs were not the only source of astrocytes in the postnatal DG, but also local astrocytes were able to divide and generate new astrocytes. Notably, such local proliferation of postnatal astrocytes has been

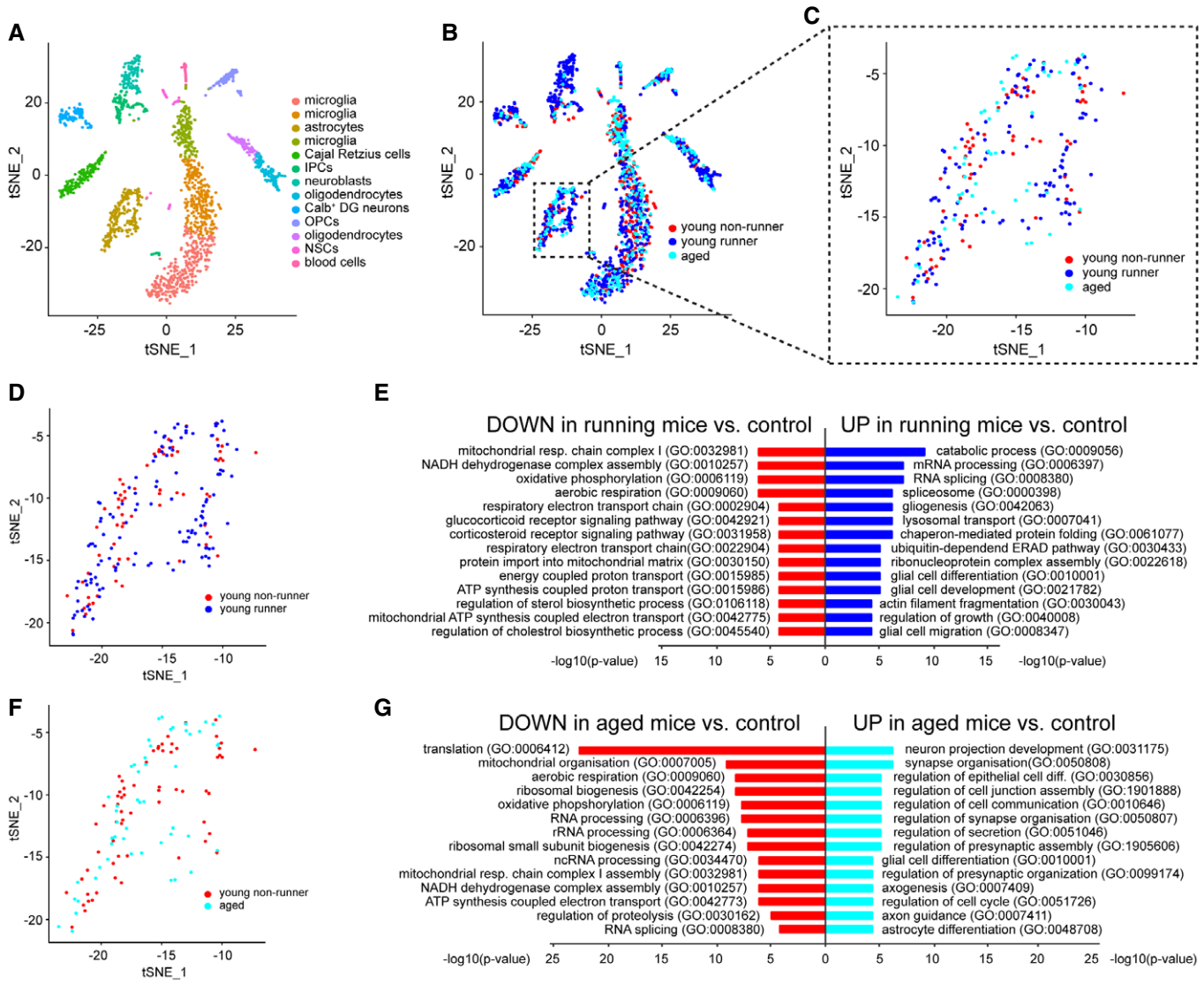

Figure 6. Molecular profile of astrocytes under pro- and anti-neurogenic conditions.

A tSNE plot of cluster analysis revealed the presence of all expected DG cell types identified by known markers.

B DG cell types were present in all three experimental conditions (young non-runner in red; young runner in dark blue; aged in light blue). Box indicates the cluster containing exclusively DG astrocytes.

C tSNE plot representing astrocytes in all three experimental conditions.

D Comparison of astrocytes derived from the DG of young non-running animals to those of young runners revealed no differential clustering between the two conditions.

E Statistical overrepresentation test by Panther; selected Gene Ontology (GO)-terms for biological processes are represented for genes downregulated (red) and upregulated (dark blue) in astrocytes from running mice.

F Comparing astrocytes from the DG of young control animals to those of aged mice did not result in differential clustering.

G Panther statistical overrepresentation test for selected GO-terms for biological processes for genes downregulated (red) and upregulated (light blue) in astrocytes derived from aged animals.

previously described for the developing neocortex and spinal cord (Ge *et al*, 2012; Tien *et al*, 2012; Shen *et al*, 2021), where it significantly contributes to the glial increase and brain growth (Bandeira *et al*, 2009). Investigating the cell type-specific proliferation potential, we observed that the vast majority of proliferating cells at P3 were rNSCs, while at later stages most proliferating cells acquired lineage-restricted precursor identity (neuronal or glial). Hence, we next asked if proliferating astrocytes and rNSCs were lineage-related. Combining fate-mapping with proliferation analysis, we identified *Nestin*$^{+}$ rNSCs as a direct source of astrocytes which further proliferate to give rise to postnatally born astrocytes. How often an astrocyte is able to divide, and to which extent these dividing astrocytes can be called precursors, as claimed for other brain regions (Zhu *et al*, 2011; Takeuchi *et al*, 2020), needs to be clarified

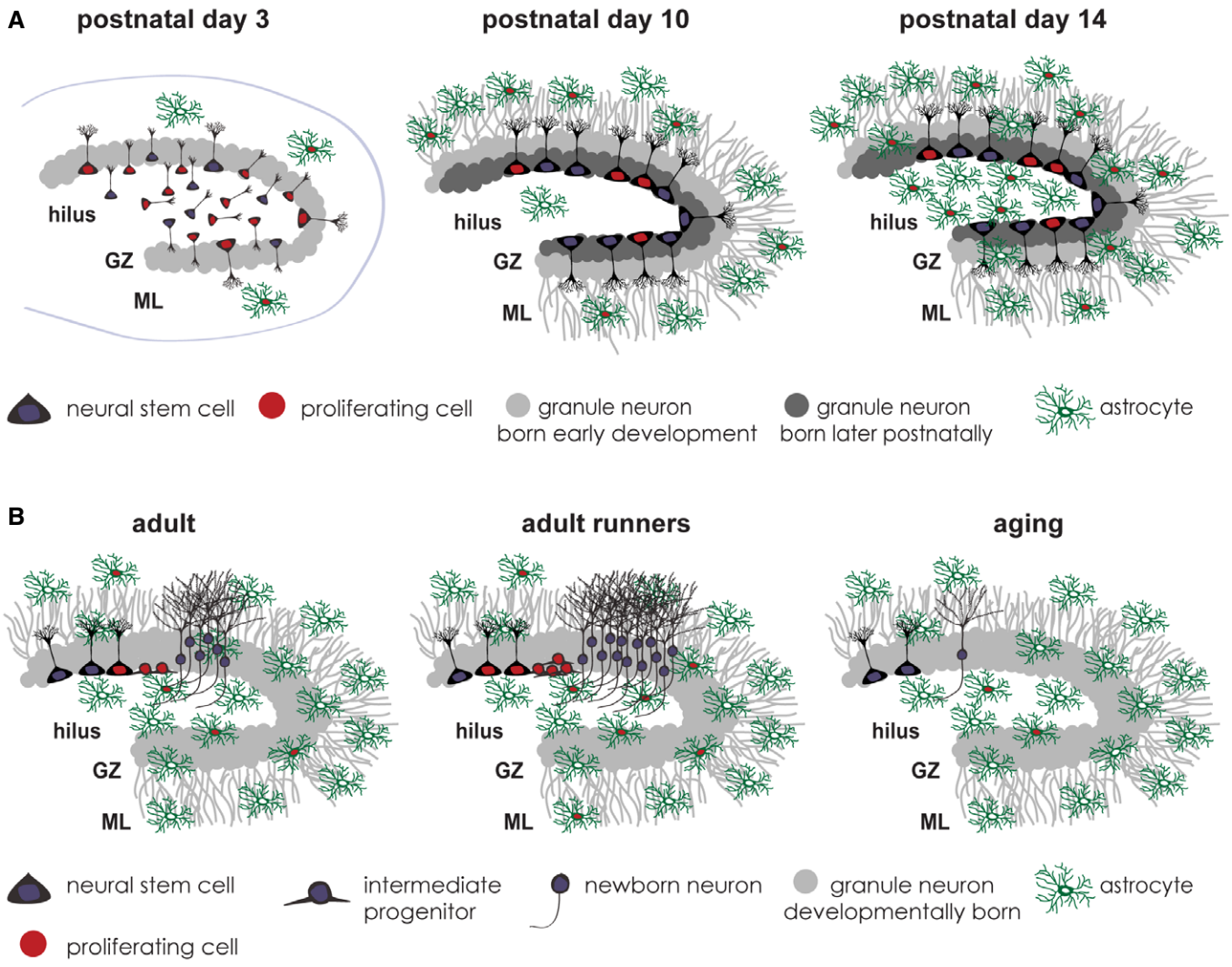

Figure 7. Summary of astrogenesis in the DG from development to aging.

A Schematics depicting the process of DG astrogenesis along postnatal development. The first astrocytes appeared as early as postnatal day 3 from perinatal neural stem cells. From P10 to P14 astrocyte numbers are constantly increasing also by local astrocyte proliferation leading to an outside-in-pattern of astrogenesis.

B Schematics showing neurogenesis and astrogenesis in the adult DG. Comparable to neurogenesis, astrogenesis is a dynamic process. Mostly driven by local astrocyte proliferation, astrogenesis is increased upon running wheel stimulus and diminished upon aging. GZ, granule zone; ML, molecular layer.

in future studies. Interestingly, our data indicated regional difference in the timing of astrogenesis within the DG, suggesting an outside-in-pattern comparable to what has been reported for DG neurons (Mathews *et al*, 2010). Since DG neurogenesis precedes astrogenesis (Brunne *et al*, 2010; Nicola *et al*, 2015; Bond *et al*, 2020) it is intriguing to speculate that the region-specific generation of astrocytes follows the maturation state of pre-existing neuronal structures: since early-born neurons layered to the outer DG compartments, this region may require the first astrocytes for further maturation. Our data demonstrate that astrocytes of all DG compartments originate from *Nestin*$^{+}$ rNSCs, and it will be interesting to investigate whether the region-specific timing of astrogenesis is a result of an intrinsic program of rNSCs or rather determined by astrocytic requirements of different DG layers at different timepoints.

A fundamental principle of neocortical development is that neurogenesis and gliogenesis are temporally segregated processes. Very recently, this concept was questioned by a study showing that neocortical rNSCs generate glial cells already from E12 onwards, suggesting a simultaneous generation of neuronal and glial cells. The observed neurogenic-to-gliogenic switch was proposed to rather reflect a downregulation of the neurogenic process as opposed to an upregulation of the glial program (Shen *et al*, 2021). In line with Bond *et al* (2020), we demonstrate here that even though neurogenesis starts already at late embryonic stages, neurogenesis and astrogenesis in the postnatal DG are not temporally segregated but occur simultaneously. This finding raises the essential question whether there is a multipotent rNSC in the postnatal DG, in which neuronal versus glial fate decisions are regulated at the single-cell level, or if

there are already fate-committed gliogenic and neurogenic rNSC populations? In case of a multipotent precursor, a simultaneous process would require an extra-precise coordination and regulation of neuro- and astrogenesis in single rNSCs (Miller & Gauthier, 2007). On the contrary, if neurogenesis and astrogenesis are driven by fate-committed rNSCs, it will be important to identify the timepoint in which those precursors are segregated. Given that neurogenesis significantly outnumbers gliogenesis at any stage of DG development, the numbers of generated neurons versus astrocytes can be either regulated by the number of fate-determined precursors or by the number of cell divisions that each precursor can undergo. Furthermore, it will be most intriguing to assess (i) to which extent the fate determination is reversible or hardwired, and (ii) whether cell fate is intrinsically determined or shaped by the extrinsic environment. Future studies should explore the mechanisms regulating timing and coordination of simultaneous neuro- and astrogenesis.

Entering adulthood, most brain regions lose their ability to generate neurons and succumb to gliogenesis, specifically oligodendrogenesis (El Waly *et al*, 2014). A key feature of the DG is that simultaneous neurogenesis and astrogenesis persist life-long. Work of the past decades identified numerous signaling pathways, transcriptional, epigenetic, and metabolic regulators that exert tight control over the production of new neurons from resident stem cells (Beckervordersandforth *et al*, 2015; Bond *et al*, 2015; Kempermann *et al*, 2015; Beckervordersandforth, 2017). Even though the generation of new astrocytes by adult rNSCs has been described more than a decade ago (Suh *et al*, 2007; Bonaguidi *et al*, 2011; Encinas *et al*, 2011), a comprehensive analysis of adult rNSC lineage progression by intravital live imaging did not identify the generation of new astrocytes by different rNSCs populations (*Ascl1*$^+$, *Gli1*$^+$; (Pilz *et al*, 2018; Bottes *et al*, 2021)). These seemingly contradictory results may be explained by several underlying causes. First, rNSCs are heterogenous: while *Sox2*- and *Nestin*-expressing rNSCs have been reported to give rise to adult-born astrocytes (Suh *et al*, 2007; Bonaguidi *et al*, 2011), *Ascl1*- and *Gli1*-expressing rNSCs do not (Pilz *et al*, 2018; Bottes *et al*, 2021). Second, adult astrogenesis is strongly overwhelmed by adult neurogenesis, suggesting that the numbers of rNSC clones that have been consistently imaged were not enough to capture such a rare event like rNSC-derived astrogenesis (Pilz *et al*, 2018; Bottes *et al*, 2021). Third, rNSCs are not the primary source of new astrocytes in the adult brain. In fact, we observed locally proliferating astrocytes in all compartments of the adult DG that were able to divide 1–2 times over a period of 9 days, thereby matching previously reported astrocyte divisions in the postnatal cortex (Ge *et al*, 2012). These proliferating astrocytes are the main drivers of adult astrogenesis. Interestingly, adult rNSCs were able to give rise to astrocytes which further proliferated corroborating a direct lineage relation as described for postnatal development. Overall, our work opens up a variety of questions that needs to be addressed by future research: is every astrocyte in principle able to proliferate or is this a unique property of a specific astrocyte subpopulation? What triggers an astrocytic division? Is this driven by intrinsic or extrinsic signals or both?

Voluntary physical activity is the most potent known stimulus to enhance adult neurogenesis in the DG (van Praag *et al*, 1999a, 1999b) and leads to increased cognitive abilities and improved mood in animals and in humans (van Praag, 2008). Intriguingly, we observed a significant increase in adult astrogenesis upon running wheel stimulus, which was driven by increased proliferation of local astrocytes. Together with evidence that enriched environment, another pro-neurogenic stimulus, evokes a similar increase in astrogenesis (Williamson *et al*, 2012; Singhal *et al*, 2020), our data suggest that adult astrogenesis is a dynamic process able to adapt to environmental stimuli (Fig 7B). However, even though total numbers increased, the percentage of neurons and astrocytes among all newly generated cells did not differ between standard housing conditions and running wheel. Even more, this ratio matched the overall occurrence of neurons and astrocytes in the adult DG, indicating a tightly regulated balance between both cell types under different conditions. Since astrocytes are responsible for metabolic and structural support, as well as proper rNSC function and neuronal maturation (Song *et al*, 2002; Lie *et al*, 2005; Perea & Araque, 2007; Suzuki *et al*, 2011; Araque *et al*, 2014; Ehret *et al*, 2015), one can hypothesize that a continuous supplement of neurons also requires more astrocytes to maintain proper niche function. This raises the intriguing possibility that not only neurogenesis but also astrogenesis may significantly contribute to hippocampal plasticity upon complex behavioral stimuli. A key question here is which mechanisms regulate astrogenesis? According to a recent publication, astrogenesis in the adult diencephalon is mediated by SMAD4-signaling (Ohlig *et al*, 2021). SMAD4 is a transcription factor downstream of the TGFβ and BMP signaling pathways (Luo, 2017), which is involved in the regulation of rNSC functions (Mira *et al*, 2010) and astrocyte differentiation (Mabie *et al*, 1997; Stipursky *et al*, 2014), and it is tempting to speculate that SMAD4 also plays a role in DG astrogenesis. Notably, voluntary exercise induced the upregulation of many genes involved in gliogenesis, glial cell differentiation, and migration, including the pro-astrocytic transcription factors (*Stat3*, *Sox9*, and *Id4*), components of Notch and Sonic hedgehog (Shh) signaling pathways (*Hes1*, *Hes5*, *Shh*, and *Smo*) as well as receptors for growth factors (*Fgfr2*). Of note, scRNA-seq by 10X Genomics captures predominantly highly expressed genes, and cell isolation per se may induce transcriptional changes (van den Brink *et al*, 2017), emphasizing the need to validate candidate factors by orthogonal methods such as *in situ* hybridization. Nevertheless, all of these represent well-suited candidates for regulating the enhanced proliferation of local astrocytes, and it will be interesting to address their functions in future studies.

Aging is a systemic degenerative process and is associated with a decrease in the regenerative properties. Upon aging, a massive decline of newly generated neurons has been described together with detrimental effects on neuronal maturation and an exhaustion of the rNSC pool (Kuhn *et al*, 1996; Seki, 2002; Garcia *et al*, 2004; Heine *et al*, 2004; Encinas *et al*, 2011). Notably, we observed that the ratio between newly generated neurons and astrocytes was shifted in aging animals toward astrogenesis. This was predominantly mediated by a dramatic decrease in neurogenesis and not by an increase in astrogenesis. In fact, we observed an overall decrease in astrogenesis upon aging, but the decrease was significantly milder (50%) than the decline of neurogenesis (95%). Also under pathological conditions, the production rate of neurons and astrocytes by rNSCs is shifted in favor of astrocytes (Woodbury *et al*, 2015). These astrocytes may not necessarily derive from astrocytic divisions, but rather from terminal differentiation of rNSCs into astrocytes as suggested by the "disposable stem cell model" (Encinas *et al*, 2011). Here, we report that replenishment of the

astrocytic compartment in aging animals is also driven by a substantial number of dividing astrocytes. Why does the aging niche still undertake the effort to produce new astrocytes while neurogenesis is seized up? Interestingly, scRNA-seq analysis revealed that many genes potentially upregulated in astrocytes of the aging DG appeared to be involved in synapse organization, presynaptic assembly, axogenesis, and axon guidance. This suggests that astrocytes in the aged DG may be rather maintaining synaptic connection and stabilizing existing neural circuitries than forming new synapses to integrate newborn neurons into DG circuitries. Here, it is interesting to note that scRNA-seq analysis of aging astrocytes from non-neurogenic brain regions identified genes involved in synapse elimination (Boisvert *et al*, 2018). To which extent this discrepancy may be explained by the specific plasticity of the hippocampal niche will be interesting to reveal in future studies. Moreover, GO-term analysis hinted toward enhanced regulation of cell communication and cell junction assembly which let us to speculate that a key purpose of astrocytes in the aging DG may be to preserve existing cellular structures to counteract aging-induced degenerative processes.

This discussion highlights the necessity of shedding light on the processes of astrogenesis and its regulation as many questions remain pending. Using the DG as a model system, we here provide a comprehensive description of astrogenesis from development to age. Our work serves as a sound basis to functionally assess astrocyte generation and dynamics under neurodevelopmental, neurodegenerative, and neuropsychiatric disease conditions. A comprehensive understanding of the contribution of astrogenesis to the pathology of such diseases will help to develop novel astrocyte-based treatment options.

Materials and Methods

Reagents and Tools table

Reagent/Resource	Reference or Source	Identifier or Catalog Number
Experimental models		
*Nestin*CreER^{T2}; CAG CAT GFP *(Mus Musculus)*	Nakamura *et al* (2006); Yamaguchi *et al* (2000)	
*Nestin*CreER^{T2}; YFP *(Mus Musculus)*	Yamaguchi *et al* (2000); Srinivas *et al* (2001)	
*hGFAP*eGFP *(Mus Musculus)*	Nolte *et al* (2001)	
hGFAP-RFP *(Mus Musculus)*	Hirrlinger *et al* (2005)	
Antibodies		
Primary antibodies (dilution; required pre-treatment); in vivo		RRID
Rabbit anti-ACSBG1 (1:400; antigen retrieval)	Abcam	AB_2222394
Rabbit anti-ALDH1L1 (1:400; antigen retieval)	Abcam	AB_10712968
Rat anti-BrdU (1:200; BrdU pre-treatment)	Serotec	AB_609566
Guinea pig anti-DCX (1:1,000)	Millipore	AB_304558
Chicken anti-GFAP (1:500)	Abcam	AB_304558
Mouse anti-GFAP (1:500)	Merck	AB_477010
Rabbit anti-GFAP (1:500)	Agilent	AB_2811722
Chicken anti-GFP (1:500)	Aves	AB_10000240
Goat anti-GFP (1:500)	Scigen	AB_2333101
rat anti-KI67 (1:100)	Thermo Fisher Scientific	AB_10854564
Mouse anti-MCM2 (1:500; antigen retrieval)	BD Bioscience	AB_2141952
Rabbit anti-MCM2 (1:500)	Cell Signalling Technologies	AB_2142137
Chicken anti-NESTIN (1:500)	Aves	AB_10805379
Mouse anti-NESTIN (1:300)	Merck	AB_94911
Mouse anti-NEUN (1:100)	Merck	AB_2298772
Mouse anti-S100β (1:500)	Merck	AB_2665776
Goat anti-SOX2 (1:300)	Santa Cruz	AB_2286684
Rat anti-TBR2 (1:250; antigen retrieval)	Thermo Fisher Scientific	AB_11042577

Reagents and Tools table (continued)

Reagent/Resource	Reference or Source	Identifier or Catalog Number
Primary antibodies (dilution; required pre-treatment); in vitro		RRID
Mouse anti-GFAP (1:200)	Sigma-Aldrich	AB_477010
Mouse anti-βIII-TUBULIN (1:1,000)	Sigma-Aldrich	AB_477590
Secondary antibodies (dilution: all 1:400; host: donkey); in vivo		Cat. Number and/or RRID
α-rabbit Alexa405	Abcam	ab175649; AB_2715515
α-mouse Alexa405	ThermoFisher Scientific	A48257; AB_2884884
α-goat Alexa405	ThermoFisher Scientific	A48259; AB_2890272
α-mouse Alexa488	Jackson ImunoResearch Laboratories	715-545-150; AB_2340846
α-goat Alexa488	ThermoFischer Scientific r	A-11055; AB_2534102
α-rabbit Alexa488	Jackson ImunoResearch Laboratories	711-545-152; AB_2313584
Streptavidin conjugated Alexa488	ThermoFischer Scientific	S11223; not available
α-mouse Alexa647	Biolegend	406414; AB_2563202
α-chicken Alexa647	Jackson ImunoResearch Laboratories	703-605-155; AB_2340379
α-chicken Biotin	Jackson ImunoResearch Laboratories	703-065-155; AB_2313596
α-goat Biotin	Jackson ImunoResearch Laboratories	705-065-147; AB_2340397
α-chicken CF488A	Biotium	20166; AB_10854387
α-guinea pig CF633	Biotium	20171; AB_10852673
α-mouse Cy3	Jackson ImunoResearch Laboratories	715-165-150; AB_2340813
α-rabbit Cy3	Jackson ImunoResearch Laboratories	711-165-152; AB_2307443
α-rat Cy3	Jackson ImunoResearch Laboratories	712-165-153; AB_2340667
α-chicken Cy3	Jackson ImunoResearch Laboratories	703-166-155; AB_2340364
α-goat Cy3	Jackson ImunoResearch Laboratories	705-165-147; AB_2307351
α-guinea pig Cy3	Jackson ImunoResearch Laboratories	706-165-148; AB_2340460
Streptavidin conjugated Cy3	Jackson ImunoResearch Laboratories	016-160-084; AB_2337244
α-rat Cy5	Jackson ImunoResearch Laboratories	712-175-153; AB_2340672
α-rabbit Cy5	Jackson ImunoResearch Laboratories	711-175-152; AB_2340607
α-mouse Cy5	Jackson ImunoResearch Laboratories	715-175-151; AB_2340820
α-guinea pig FITC	Jackson ImunoResearch Laboratories	706-095-148; AB_2340453
Secondary antibodies (dilution: all 1:400; host: donkey); in vitro		Cat. Number and/or RRID
α-mouse Alexa Fluor 488 (1:1,000)	Thermo Fisher Scientific	A-21141; AB_2535778
α-mouse Alexa Fluor 647 (1:500)	Thermo Fisher Scientific	A-21240; AB_2535809

Reagents and Tools table (continued)

Reagent/Resource	Reference or Source	Identifier or Catalog Number
Oligonucleotides and sequence-based reagents		
Mouse line	**Primer sequence**	
*Nestin*CreER^{T2}	fwdGTTTCACTGGTTATGCGGCG	
	revGAGTTGCTTCAAAAATCCCTTCC	
CAG CAT GFP	fwdCTGCTAACCATGTTCATGCC	
	revGGTACATTGAGCAACTGACTG	
YFP	fwdAAAGTCGCTCTGAGTTGTTAT	
	revWTGGAGCGGGAGAAATGGATATG	
*hGFAP*eGFP	fwdCAGGTTGGAGAGGAGACGCATCA,	
	revCAGCTTGTGCCCCAGGATGT	
hGFAP-RFP	mRFP4110: CCCCGTAATGCAGAAGAAG	
	mRFP4111: CTTGGCCATGTAGGTGGTCT	
Chemicals, enzymes and other reagents		
4´,6-diamidino-2-phenylindole (DAPI)	Sigma Aldrich	D8417
Aqua Poly/Mount	Polysciences	18606
B27	Thermo Fisher Scientific	17504044
Bromodeoxyuridine	Sigma-Aldrich	B5002
L-Glutamine	Sigma-Aldrich	G8540
HEPES	Sigma Aldrich	H3375
Hyaluronidase	Sigma-Aldrich	H3884-100mg
Paraformaldehyde	Carl Roth	335
Penicillin	Sigma-Aldrich	A5955
Poly-D-lysine	Biochrom AG	L7240
Sunflower seed oil	Sigma-Aldrich	S5007
Tamoxifen	Sigma-Aldrich	T5648
TissueTec	Leica Biosytem	14020108926
Triton X-100	Carl Roth	3051
Trypsin	Sigma-Aldrich	T9201-500mg
Trypsin/EDTA	Gibco	11560626
Tween 20	Sigma-Aldrich	P9416
Software		
Adobe Illustrator	Adobe	https://www.adobe.com/creativecloud.html
AxioVision 4.7 software	Carl Zeiss	https://www.micro-shop.zeiss.com/de/de/system/axiovision+software-software+axiovision-software/6014/
Fiji ImageJ	Schindelin *et al* (2012)	https://fiji.sc
GraphPad Prism 9.0	Graphpad Software, Inc	https://www.graphpad.com/scientific-software/prism
Panther online tool	Mi *et al* (2019)	http://www.pantherdb.org
Seurat R package (version 3.1.0)	Butler *et al* (2018); Stuart *et al* (2019)	
TTT for single cell tracking	Hilsenbeck *et al* (2016)	
Other		
AAV2/9-hsyn-jGCaMP7s-WPRE	AddGene	104487
ApoTome.2 (Axio Observer 7; Axiocam 503; Colibri 7 LED light source)	Carl Zeiss	NA
Cell observer	Carl Zeiss	NA

Reagents and Tools table (continued)

Reagent/Resource	Reference or Source	Identifier or Catalog Number
Cell Ranger (version 2.1.1)	10X Genomics, Pleasanton, CA	NA
Chromium Controller and the Chromium Single Cell 3' Reagent Kit v2	10X Genomics, Pleasanton, CA	NA
Cryotome	Leica Microsystems	NA
Dental cement	Superbond C&B, Sun Medical	170447
FastQC (version 0.11.8)	Babraham bioinformatics	NA
Leica SP8 MP microscope	Spectra Physics	NA
Sliding microtome	Leica Microsystems	NA
Superglue	Pattex ultra, Henkel	NA
Zeiss LSM 780 confocal microscope	Carl Zeiss	NA

Methods and Protocols

Experimental model and subjected details

All experiments were carried out in accordance with the European Communities Council Directive (86/609/EEC). Animal experiments were approved by the Government of Middle-Franconia and Upper Bavaria. If not further specified, mice were group-housed in standard cages with *ad libitum* access to food and water under a 12-h light/dark cycle. Only mice used for the running paradigm were held singly in standard cages with additional access to a running wheel. Distance of running was precisely measured by tachometers attached to the running wheels (Conrad Digispeed 5, Cat#853147). During development, *Nestin*-CreER^{T2}; GFP animals (Yamaguchi *et al*, 2000; Nakamura *et al*, 2006) were used for fate-mapping, birth-dating, and proliferation experiments. 8-week-, 14-month-, and 21-month-old *hGFAP*eGFP animals (Nolte *et al*, 2001) were used to investigate astrogenesis and neurogenesis by BrdU birth-dating in the adult and aging DG. To further confirm adult astrogenesis, 9-week-old *Nestin*-CreER^{T2}; Rosa26YFP animals (Yamaguchi *et al*, 2000; Srinivas *et al*, 2001) were analyzed. Adult and aging fate-mapping experiments were conducted in *Nestin*CreER^{T2}; GFP animals. *In vivo* and *in vitro* imaging experiments were carried out in *hGFAP*-RFP mice (Hirrlinger *et al*, 2005). Male and female mice were used for experiments. Whenever possible, gender-matched mice from one litter were randomly assigned to treatments to correct for batch biases. All animals have been described previously, and all efforts were made to minimize the number of animals used, and their suffering.

Genotyping

Genotyping of transgenic mice was performed using polymerase chain reaction (PCR) from DNA extracted from small tissue samples (ear biopsies). The following primers were used for genotyping:

*Nestin*CreER^{T2}: fwd GTTTCACTGGTTATGCGGCG, rev GAGTT GCTTCAAAAATCCCTTCC; CAG CAT GFP: fwd CTGCTAACCATG TTCATGCC, rev GGTACATTGAGCAACTGACTG; Rosa26YFP: fwd AAAGTCGCTCTGAGTTGTTAT, rev GGAGCGGGAGAAATGGATAT G, *hGFAP*eGFP: fwd CAGGTTGGAGAGGAGACGCATCA, rev CAGCT TGTGCCCCAGGATGT *hGFAP*-RFP: mRFP 4110: CCCCGTAATGCA GAAGAAGA, mRFP 4111: CTTGGCCATGTAGGTGGTCT.

Tamoxifen administration

Tamoxifen (Sigma-Aldrich, Cat# T5648) was dissolved at a concentration of 10 mg/ml in 10% ethanol and 90% sunflower seed oil under constant agitation in the dark at room temperature. To induce recombination, perinatal (P0) mice were subcutaneously injected with freshly prepared 40 mg/kg tamoxifen twice (12 h apart). 8-week-old, 14-month-old, and 21-month-old animals were intraperitoneally injected with freshly prepared 40 mg/kg tamoxifen every 12 h for five consecutive days.

BrdU administration

Bromodeoxyuridine (BrdU, Sigma-Aldrich, Cat# B5002) was dissolved in sterile 0.9% NaCl solution at a concentration of 10 mg/ml. For developmental birth-dating experiments, P3, P7, P14, and P21 animals were intraperitoneally injected once with 50 mg/kg BrdU. For adult birth-dating experiments, BrdU (1 mg/ml) was dissolved together with 2% sucrose in drinking water. BrdU water was held in the dark and changed every 4 days during the experiment.

Tissue processing

To collect brain tissue from mice of different ages, the animals were killed and fixed with paraformaldehyde (PFA) by transcardial perfusion, except perinatal stage P3. Killing of the animals occurred in dependence of their age: P3 mice were killed by decapitation, P7 and P10 mice were killed by isoflurane, and from P14 onwards mice were killed using CO_2. Transcardial perfusion was conducted by first flushing with phosphate-buffered saline (PBS, pH 7.4) for 5 min at a flow rate of 10 ml/min followed by fixation with 4% PFA (Roth, Cat# 0335) in 0.1 mM phosphate buffer (pH 7.4) for 5 min at a flow rate of 10 ml/min. P7 animals were transcardially perfused using syringes filled with 10 ml PBS (pH 7.4) and subsequently fixed with 10 ml 4% PFA in 0.1 mM phosphate buffer (pH 7.4). For brain tissue collection from P3 mice, no transcardial perfusion occurred. Instead, the brains were removed and fixed in 4% PFA overnight. All PFA-fixed brains were dehydrated and stored at 4°C in 30% sucrose solution.

For further processing, brain tissue from P3 and P7 animals was immersed in cryostat embedding medium and subsequently frozen using dry ice. The frozen brain tissue was cut into 16-µm-thick sections using a cryotome (Leica Microsystems, Wetzlar, Germany).

Cut sections were immediately transferred to coated adhesive glass slides, which were then air-dried for 2 h at room temperature (RT) and then stored at −20°C. From P10 onwards, brain tissue was coronally cut into 50-µm sections using a sliding microtome (Leica Microsystems, Wetzlar, Germany). Cut sections were stored at −20°C in cryoprotection solution filled 96-well plates.

Histology

Immunofluorescent stainings were performed either on mounted (P3, P7) or free-floating sections (from P10 onwards). All slices were washed 3 times for 15 min with 1×PBS and then incubated with primary antibodies diluted in blocking solution (1×PBS/3% normal donkey serum/0.05% TritonX100) at 4°C for 72 h.

The following primary antibodies were used: rabbit anti-ALDH1L1 (1:500, Abcam, AB_10712968), rabbit anti-ACSBG1 (1:400, Abcam, AB_2222394), rat anti-BrdU (1:200, Serotec, AB_609566), guinea pig anti-DCX (1:1,000, Millipore, AB_304558), chicken anti-GFAP (1:500, Abcam, AB_304558), mouse anti-GFAP (1:500, Merck, AB_477010), rabbit anti-GFAP (1:500, Agilent, AB_2811722), chicken anti-GFP (1:500, Aves, AB_10000240), goat anti-GFP (1:500, Scigen, AB_2333101), rat anti-KI67 (1:100, Thermo Fisher Scientific, AB_10854564), mouse anti-MCM2 (1:500, BD Bioscience, AB_2141952), rabbit anti-MCM2 (1:500, Cell Signalling Technologies, AB_2142137), chicken anti-NESTIN (1:500, Aves, AB_10805379), mouse anti-NESTIN (1:300, Merck, AB_94911), mouse anti-NEUN (1:100, Merck, AB_2298772), mouse anti-S100β (1:500, Merck, AB_2665776), goat anti-SOX2 (1:300, Santa Cruz, AB_2286684), rat anti-TBR2 (1:250, Thermo Fisher Scientific, AB_11042577).

After removal of the primary antibodies, the sections were washed 3 times for 15 min with 1× PBS before incubation with fluorescent secondary antibodies. All secondary antibodies were diluted in blocking solution at a concentration of 1:400. The following fluorophores were conjugated to the secondary antibodies according to the species against which the primary antibodies were raised: Alexa 405 (Thermo Fisher Scientific), Alexa Fluor 488, Alexa Fluor 647, FITC, Cy3, and Cy5 (all Jackson ImmunoResearch). Sections were incubated with secondary antibodies at 4°C overnight. After removal of secondary antibody solution, sections were washed 3 times for 15 min with 1× PBS, and free-floating sections were mounted on slides. All sections were cover slipped with Aqua Poly/Mount (Polysciences, Cat# 18606). Object slides were stored at 4°C in the dark.

For immunostainings against ACSBG1, MCM2 (ms), ALDH1L1, and TBR2, sections were subjected to antigen retrieval. Therefore, sections were treated with 1 M Tris/EDTA (pH 9) for 5 min at 99°C before the primary antibody was incubated. After the heating step, sections were allowed to cool down for 20 min and washed 3 times for 10 min with MilliQ water, followed by 3 times washing for 10 min with 1×PBS. Immunofluorescent stainings for ACSBG1, MCM2, ALDH1L1, and TBR2 were performed as described above.

Immunohistochemistry against BrdU requires loosening of the tight DNA structure to allow the BrdU antibody to bind to its antigen. Therefore, we pre-treated the sections with 2 N HCl for 10 min at 37°C. For neutralization, sections were afterwards incubated in 0.1 M borate buffer for 10 min at RT and rinsed three times in 1× PBS. Fluorescent staining for the BrdU antibody was performed as described above. Importantly, if BrdU immunohistochemistry was combined with other markers, their antibody stainings have to be finished before the sections were treated with HCl and borate buffer.

To better visualize the GFP reporter in slices of *Nestin*CreER^{T2}; GFP mice, we used an additional signal amplification step. After incubation with the primary antibody against GFP, a biotinylated secondary antibody (1:400; Vector Laboratories) was incubated at 4°C overnight. After removal, the sections were rinsed 3 times for 15 min with 1× PBS at RT, followed by incubation of a fluorophore-conjugated streptavidin (1:400; Invitrogen) in blocking solution overnight at 4°C. The staining procedure was finished as described above.

Microscopy

All images shown and quantified in this study were taken at the confocal microscope, expect images analyzed for the fate-mapping studies by *Nestin*CreER^{T2}; GFP mice in the adult and aging brain. Confocal images were taken at the Zeiss LSM 780 confocal microscope (Carl Zeiss), which was equipped with four lasers (405, 488, 559, and 633 nm) and 40× (NA 1.46) and 63× (NA 1.4) oil immersion objective lenses. Z-stack thickness differed according to the age of experimental animals: 10–12 µm (P3–P7), 20–25 µm (P10–P14), and 35–40 µm (from P28 onwards). For quantification, the 40× oil immersion objective was used, and the step size between z-stacks was always 2 µm. Representative pictures and single cells were captured with 63× oil immersion objective with a z-stack size of 1 µm. All confocal images were captured with standard settings: The number of total pixels per image and the color depth were set to 1024 × 1024 and 16 bit, respectively.

For adult and aging fate-mapping experiments, quantification images were taken using a Zeiss inverted Axio Observer 7 with ApoTome.2 equipped with an Axiocam 503, a Colibri 7 LED light source and 20× objective (NA 0.8). Z-stack thickness was 35–40 µm with a steps size of 2 µm. Apotome images were obtained with the standard number of total pixels and the color depth of 1936 × 1460 and 16 bit, respectively. All images were processed using Fiji ImageJ (Schindelin *et al*, 2012). No additional ImageJ plugins were used.

Quantification and statistical analysis

Quantification of total cell numbers

Quantification of total cell numbers was conducted using confocal images of 3–4 sections containing DGs from 3–6 different animals. The exact values of biological replicates (n) are depicted in the tables. Co-expression of cell type-specific protein expression with markers for generation (BrdU), proliferation (KI67/MCM2), and recombination (GFP) was manually counted and calculated per area, which was measured using the ImageJ software. Differences in z-stack thickness were included in the calculation per area. The investigator was blinded during the assessment of the results. Only animal identification numbers were visible, but no treatment information.

Statistical analysis

Data were analyzed using GraphPad Prism 9.0. Following normal distribution, two-sample comparisons were conducted by using unpaired Student's t-tests, and multiple comparisons were performed by one-way ANOVA followed by a Tukey *post hoc* test. The statistical significance level α was set to 0.05. The results are

represented as mean ± SEM. The number of biological replicates (n) is specified for each analysis in the tables.

In vitro imaging of SEZ-derived NSC-cultures

SEZ cell culture

SEZ cultures were prepared from the adult SEZ of young adult (8–12 weeks) *hGFAP*-RFP mice. Briefly, the tissue was enzymatically dissociated in 0.7 mg/ml hyaluronic acid (Sigma-Aldrich) and 1.33 mg/ml trypsin (Sigma-Aldrich) in Hanks' Balanced Salt Solution (HBSS; Invitrogen) with 2 mM glucose at 37°C for 30 min. Dissociation was stopped by adding an equal volume of an ice-cold medium consisting of 4% bovine serum albumin (BSA; Sigma-Aldrich) in Earle's Balanced Salt Solution (EBSS; Invitrogen), buffered with 20 mM HEPES (Invitrogen). Cells were then centrifuged at 200 *g* for 5 min, resuspended in ice-cold medium consisting of 0.9 M sucrose (Sigma-Aldrich) in 0.5× HBSS, and centrifuged for 10 min at 750 *g*. The cell pellet was resuspended in 2 ml ice-cold medium consisting of 4% BSA in EBSS buffered with 2 mM HEPES, and the cell suspension was placed on top of 12 ml of the same medium and centrifuged for 7 min at 200 *g*. The cell pellet was finally resuspended in DMEM/F12 Glutamax (Gibco) supplemented with B27 (Thermo Fisher Scientific), 2 mM glutamine (Sigma), 100 units/ml penicillin (Sigma-Aldrich), 100 µg/ml streptomycin (Invitrogen), buffered with 8 mM HEPES (Sigma-Aldrich), and cells were plated on poly-D-lysine (Biochrom AG) coated coverslips at a density of 200–300 cells per mm^2.

Immunocytochemistry

Cell cultures were fixed in 4% PFA in PBS for 15 min at room temperature and processed for antibody staining. Antibodies used were as follows: mouse IgG2b anti-βIII-TUBULIN (1:1,000; Sigma-Aldrich) and mouse anti-GFAP (1:500; Sigma-Aldrich). Secondary antibodies were chosen according to the primary antibodies and were coupled to Alexa488 and Cy3 antibodies and coverslips were counterstained with 4′,6-diamidino-2-phenylindole (DAPI; Sigma-Aldrich).

Time-lapse video microscopy

Time-lapse video microscopy and single-cell tracking of primary SEZ cultures (Schroeder, 2008; Ortega *et al*, 2013; Ortega & Costa, 2016; Gómez-Villafuertes *et al*, 2017; Paniagua-Herranz *et al*, 2020) was performed with a cell observer (Carl Zeiss) at a constant temperature of 37°C and 8% CO_2. Phase contrast images were acquired every 5 min for 6–10 days using a 20× phase contrast objective (Zeiss), an AxioCamHRm camera and a Zeiss AxioVision 4.7 software.

Single-cell tracking

Once the time-lapse video microscopy was over, the images exported were converted to the format required. Instructions for the correct processing of images are available for download at: https://www.bsse.ethz.ch/csd/software/tTt-and-qtfy.html. Single-cell tracking was performed using a self-written computer program [TTT; (Hilsenbeck *et al*, 2016)]. After selecting the position to be tracked and loading all the images of that position, the "Movie Window" and the "Cell Editor Window" appear. In the "Cell Editor Window" wavelength 0 corresponds to brightfield, 1 to FITC, 2 to Cy3, and 3 to DAPI. Once the wavelength 0 was selected, the single-cell tracking was performed in the "Movie Window," following the Tracking Tool instructions. In this window, different buttons are available to monitor the cell division, cell apoptosis, and lost cell. In the "Cell Editor Window," these specific cell events will be shown in the lineage tree drawn while the experiment is tracked. After tracking the clone, the nature of the cell progeny was identified by matching the brightfield pictures with the immunofluorescence images (channel 1 represented βIII-TUBULIN, channel 2 GFAP, and channel 3 for DAPI). Movies were assembled using Image J 1.42q (National Institute of Health, USA) software and are played at speed of 1 and 2 frames per second.

Intravital two-photon imaging of the adult hippocampus

Hippocampal window surgery

The hippocampal window surgery procedure was performed as described earlier (Gu *et al*, 2014; Ulivi *et al*, 2019). Briefly, 5.5-month-old female mice were anesthetized with MMF (Medetomidine 0.5 mg/kg, Midazolam 5.0 mg/kg, and Fentanyl 0.05 mg/kg) intraperitoneally. 30 min before the surgery, analgesia (Metacam 1 mg/kg and Metamizol 200 mg/kg) was administered orally. The mice were placed on a heating pad set to 37°C and fixed in a stereotactic frame. After shaving and disinfecting the skin using iodine solution (Betadine), a sagittal scalp incision was made. A 3-mm circular craniotomy was made using a dental drill, centered 1.6 mm posterior and 1.6 mm lateral from the midline. The cortex underneath the craniotomy was aspired using a 27 G blunt needle, while flushing the area with ice-chilled saline. The alveus of the hippocampus was left intact. 500 nl of AAV2/9-hsyn-jGCaMP7s-WPRE (AddGene) diluted 1:10 in saline was injected at a depth of 0.3 and 0.7 mm below the alveus using a glass micropipette. The imaging cannula, consisting of 3 × 1.5 mm steel cannula with a 3-mm glass coverslip attached with superglue (Pattex ultra, Henkel), was inserted into the craniotomy and secured with dental cement (Superbond C&B, Sun Medical). A custom-made metal headbar was attached to the skull with dental cement. Analgesia (Metacam) was administered orally 24, 48, and 78 h after the surgery. All procedures occurred in agreement with animal protocols approved by the government of Upper Bavaria.

In vivo *two-photon imaging*

In vivo two-photon imaging followed 4 weeks after the surgery. For the imaging, mice were anesthetized with MMF intraperitoneally and positioned underneath the microscope on a heating pad. Multiphoton microscopy was performed at the Core Facility Bioimaging of the Biomedical Center with a Leica SP8 MP microscope, equipped with a pulsed InSight DS+ laser (Spectra Physics). GFP and RFP excitation was achieved at 910 nm and 1,075 nm, respectively. The objective used was HC IRAPO L 25×/1.00. Voxel size was 0.3 × 0.3 × 5.0 µm, and image dimensions were 1024 × 1024 and field of view measured 306 × 306 µm. Imaging of the same area was performed at day 1, 6, and 9.

Single-cell RNA sequencing and analysis

Single-cell isolation of DG tissue and library preparation

After cervical dislocation, brains were isolated from *hGFAP*eGFP mice (2–14-month-old) and the DGs were dissected in ice-cold HBSS or PBS. Tissue was enzymatically dissociated with 0.25% Trypsin/EDTA (Gibco) in HBSS containing 2 mM Glucose at 37°C for

30 min. Before and after incubation, the tissue was repeatedly triturated with a fire-polished Pasteur pipette. Enzyme activity was stopped by the addition of equal volume of 4% BSA in Earle's Balanced Salt Solution (EBSS, Gibco). The cell suspension was filtered through a 70-µm cell strainer and centrifuged at 180 *g* for 5 min, and the pellet was resuspended in 0.9 M sucrose in 0.5× HBSS (Gibco). After further centrifugation for 10 min at 290 *g*, the cell pellet was resuspended in 2 ml of Solution 3 and placed on top of 10 ml Solution 3, centrifuged again for 7 min at 130 *g*. The resulting pellet was then resuspended in filtered PBS. Tissue preparation is also described in (Fischer *et al*, 2011). We determined cell density using a Neubauer chamber. Libraries were prepared using the Chromium Controller and the Chromium Single Cell 3' Reagent Kit v2 (10X Genomics, Pleasanton, CA) according to the manufacturers' instructions. Single-cell suspensions were diluted in nuclease-free water according to the manufacturers' instructions to obtain a targeted cell count of 5,000. Libraries were sequenced as described previously (Lukassen *et al*, 2018).

Data processing for scRNA-seq analysis using cell ranger and seurat

The reads were de-multiplexed using Cell Ranger (version 2.1.1, 10X Genomics). Mkfastg and read quality was determined by FastQC (version 0.11.8, Babraham bioinformatics). The standard Cell Ranger workflow was used for mapping the reads to the mm10 genome (10X Reference 2.1.0, GRCm38, Ensembl 84) and to identify single cells. Common quality control measures for scRNA-seq (gene count per cell, UMI count per cell, percent of mitochondrial transcripts) were calculated using the Seurat R package (version 3.1.0) (Butler *et al*, 2018; Stuart *et al*, 2019). The analyses were performed for each condition. Quality control thresholds were set to 100–2,500 genes per cells and < 10% of mitochondrial transcripts. All samples were used for further analysis.

scRNA-Seq clustering and differential gene expression analysis using Seurat

Clustering of the cells was performed using the Seurat packages for R following the vignettes of the authors (Guided tutorial—2700 PBMCs for PCA approach, version 3.1.0) (Butler *et al*, 2018; Stuart *et al*, 2019). Cluster identity was defined using known marker expression, and astrocytes were identified by the expression of astrocytic markers, that is, *Aldoc*, *Aldh1L1*, *Sox9 Slc1a2*, and *Slc1a3*. Differentially expressed genes between the different conditions were identified using the MAST algorithm as implemented in Seurat. To adjust for cellular detection rate, we used nCount_RNA as confounding variable (Finak *et al*, 2015). Very few significantly differentially expressed genes (DEGs) could be identified (determined by adjusted *P*-values). Therefore, for pathway analysis cells were selected based on their average logarithmic fold chance (avg_logFC). In the comparison of both young non-runners (ctrl) to young runners and young non-runner (ctrl) to aged non-runners, we selected genes with an avg_logFC ≥ 0.25 as being expressed at higher levels in astrocytes of ctrl animals, while genes with an avg_logFC ≤ -0.25 as being expressed at higher levels in astrocytes of running/aged mice. These genes were included for GO-term analysis using the Panther online tool (GO biological process complete) (http://www.pantherdb.org; Mi *et al*, 2019).

Data availability

The data that support the findings of this study are included in the paper and are deposited online (GEO: GSE190399, https://www.ncbi.nlm.nih.gov/geo/query/acc.cgi?acc=GSE190399).

Expanded View for this article is available online.

Acknowledgements

We thank Chichung Lie and the members of his group for helpful discussions and Chiara Rolando and Michael Wegner as members of J.S.'s thesis advisory committee for constructive comments on the project. We further thank Marlen Knobloch and Sebastian Jessberger for sharing their clonal analysis data with us, which was important to develop the initial concept of adult astrogenesis. This work was supported by grants from the German Research Foundation (DFG; BE 5136/2-1 and 1-2 to R.B., INST 410/45-1 FUGG). The research training group 2162 "Neurodevelopment and Vulnerability of the Central Nervous System" of the German Research Foundation (DFG GRK2162/1) supported this work as follows: J.S as an associated fellow and M.-T.W. and J.K. as fellows of the GRK2162. J.W. was supported by the Interdisciplinary Centre for Clinical Research (IZKF), Erlangen. S.L. was funded by the Deutsche Forschungsgemeinschaft (DFG, German Research Foundation) under Germany's Excellence Strategy within the framework of the Munich Cluster for Systems Neurology—EXC 2145 SyNergy—ID 390857198 and the Emmy Noether Programme. P.S. was supported by the Graduate School for Systemic Neurosciences GSN-LMU. Felipe Ortega acknowledges grants from the local Government of Madrid (Comunidad de Madrid, Spain) under the Multiannual Agreement with the Universidad Complutense through the Program to Stimulate Research for Young Doctors in the context of the V PRICIT (Regional Programme of Research and Technological Innovation) UCM-CAM (PR65/19-22453) and from the Spanish Ministerio de Ciencia, Innovación y Universidades (MCIU, PID2019-109155RB-I00, BFU2015-70067REDC). The present work was performed in fulfillment of the requirements for obtaining the degree "Dr. med." to Johannes Weigel. Open access funding enabled and organized by Projekt DEAL.

Author contributions

Julia Schneider: Conceptualization; Data curation; Formal analysis; Validation; Investigation; Visualization; Writing—original draft; Writing—review & editing. **Johannes Weigel:** Formal analysis; Investigation. **Marie-Theres Wittman:** Formal analysis; Investigation. **Pavel Svehla:** Formal analysis; Investigation. **Sebastian Ehrt:** Investigation. **Fang Zheng:** Investigation. **Tarek Elmzzahi:** Investigation. **Julian Karpf:** Investigation. **Lucia Paniagua-Herranz:** Investigation. **Onur Basak:** Investigation. **Arif Ekici:** Investigation. **André Reis:** Resources; Funding acquisition. **Christian Alzheimer:** Resources; Funding acquisition. **Felipe Ortega:** Resources; Supervision; Funding acquisition. **Sabine Liebscher:** Resources; Supervision; Funding acquisition. **Ruth Beckervordersandforth:** Conceptualization; Resources; Data curation; Software; Formal analysis; Supervision; Funding acquisition; Validation; Investigation; Visualization; Methodology; Writing—original draft; Project administration; Writing—review & editing.

In addition to the CRediT author contributions listed above, the contributions in detail are:

Conceptualization JS, RB; Investigation, JS, JW M-TW, PS, SE, FZ, TE, JK, LPH, OB, AE, RB; Formal analysis, JS, JW M-TW, PS, TE, LPH, RB; Resources and Funding acquisition, OB, AR, CA, FO, SL, RB; Writing-Original draft JS, RB; Supervision, FO, SL, RB. All authors read and approved the manuscript.

Disclosure and competing interests statement

All authors declare that the submitted work was performed without any personal, professional, or financial relationships that could be potentially construed as a conflict of interest.

References

Alvarez-Buylla A, Lim DA (2004) For the long run: maintaining germinal niches in the adult brain. *Neuron* 41: 683 – 686

Angevine Jr JB (1965) Time of neuron origin in the hippocampal region. An autoradiographic study in the mouse. *Exp Neurol Suppl* Suppl 2: 1 – 70

Araque A, Carmignoto G, Haydon PG, Oliet SH, Robitaille R, Volterra A (2014) Gliotransmitters travel in time and space. *Neuron* 81: 728 – 739

Attwell D, Buchan AM, Charpak S, Lauritzen M, Macvicar BA, Newman EA (2010) Glial and neuronal control of brain blood flow. *Nature* 468: 232 – 243

Ballabh P, Braun A, Nedergaard M (2004) The blood-brain barrier: an overview: structure, regulation, and clinical implications. *Neurobiol Dis* 16: 1 – 13

Bandeira F, Lent R, Herculano-Houzel S (2009) Changing numbers of neuronal and non-neuronal cells underlie postnatal brain growth in the rat. *Proc Natl Acad Sci U S A* 106: 14108 – 14113

Barres BA (2008) The mystery and magic of glia: a perspective on their roles in health and disease. *Neuron* 60: 430 – 440

Batiuk MY, Martirosyan A, Wahis J, de Vin F, Marneffe C, Kusserow C, Koeppen J, Viana JF, Oliveira JF, Voet T *et al* (2020) Identification of region-specific astrocyte subtypes at single cell resolution. *Nat Commun* 11: 1220

Bayer SA (1980) Development of the hippocampal region in the rat. I. Neurogenesis examined with 3H-thymidine autoradiography. *J Comp Neurol* 190: 87 – 114

Bayer SA, Altman J (1974) Hippocampal development in the rat: cytogenesis and morphogenesis examined with autoradiography and low-level X-irradiation. *J Comp Neurol* 158: 55 – 79

Beckervordersandforth R (2017) Mitochondrial metabolism-mediated regulation of adult neurogenesis. *Brain Plast* 3: 73 – 87

Beckervordersandforth R, Deshpande A, Schäffner I, Huttner HB, Lepier A, Lie DC, Götz M (2014) *In vivo* targeting of adult neural stem cells in the dentate gyrus by a split-cre approach. *Stem Cell Reports* 2: 153 – 162

Beckervordersandforth R, Zhang CL, Lie DC (2015) Transcription-factor-dependent control of adult hippocampal neurogenesis. *Cold Spring Harb Perspect Biol* 7: a018879

Ben Abdallah NM, Slomianka L, Vyssotski AL, Lipp HP (2010) Early age-related changes in adult hippocampal neurogenesis in C57 mice. *Neurobiol Aging* 31: 151 – 161

Berg DA, Su Y, Jimenez-Cyrus D, Patel A, Huang N, Morizet D, Lee S, Shah R, Ringeling FR, Jain R *et al* (2019) A common embryonic origin of stem cells drives developmental and adult neurogenesis. *Cell* 177: 654 – 668.e615

Boisvert MM, Erikson GA, Shokhirev MN, Allen NJ (2018) The aging astrocyte transcriptome from multiple regions of the mouse brain. *Cell Rep* 22: 269 – 285

Boldrini M, Fulmore CA, Tartt AN, Simeon LR, Pavlova I, Poposka V, Rosoklija GB, Stankov A, Arango V, Dwork AJ *et al* (2018) Human hippocampal neurogenesis persists throughout aging. *Cell Stem Cell* 22: 589 – 599.e585

Bonaguidi MA, Wheeler MA, Shapiro JS, Stadel RP, Sun GJ, Ming GL, Song H (2011) *In vivo* clonal analysis reveals self-renewing and multipotent adult neural stem cell characteristics. *Cell* 145: 1142 – 1155

Bond AM, Berg DA, Lee S, Garcia-Epelboim AS, Adusumilli VS, Ming GL, Song H (2020) Differential timing and coordination of neurogenesis and astrogenesis in developing mouse hippocampal subregions. *Brain Sci* 10: 909

Bond AM, Ming GL, Song H (2015) Adult mammalian neural stem cells and neurogenesis: five decades later. *Cell Stem Cell* 17: 385 – 395

Bondi H, Bortolotto V, Canonico PL, Grilli M (2021) Complex and regional-specific changes in the morphological complexity of GFAP(+) astrocytes in middle-aged mice. *Neurobiol Aging* 100: 59 – 71

Bondolfi L, Ermini F, Long JM, Ingram DK, Jucker M (2004) Impact of age and caloric restriction on neurogenesis in the dentate gyrus of C57BL/6 mice. *Neurobiol Aging* 25: 333 – 340

Bonthius DJ, McKim R, Koele L, Harb H, Karacay B, Mahoney J, Pantazis NJ (2004) Use of frozen sections to determine neuronal number in the murine hippocampus and neocortex using the optical disector and optical fractionator. *Brain Res Brain Res Protoc* 14: 45 – 57

Bottes S, Jaeger BN, Pilz G-A, Jörg DJ, Cole JD, Kruse M, Harris L, Korobeynyk VI, Mallona I, Helmchen F *et al* (2021) Long-term self-renewing stem cells in the adult mouse hippocampus identified by intravital imaging. *Nat Neurosci* 24: 225 – 233

van den Brink SC, Sage F, Vértesy Á, Spanjaard B, Peterson-Maduro J, Baron CS, Robin C, van Oudenaarden A (2017) Single-cell sequencing reveals dissociation-induced gene expression in tissue subpopulations. *Nat Methods* 14: 935 – 936

Brunne B, Franco S, Bouché E, Herz J, Howell BW, Pahle J, Müller U, May P, Frotscher M, Bock HH (2013) Role of the postnatal radial glial scaffold for the development of the dentate gyrus as revealed by Reelin signaling mutant mice. *Glia* 61: 1347 – 1363

Brunne B, Zhao S, Derouiche A, Herz J, May P, Frotscher M, Bock HH (2010) Origin, maturation, and astroglial transformation of secondary radial glial cells in the developing dentate gyrus. *Glia* 58: 1553 – 1569

Butler A, Hoffman P, Smibert P, Papalexi E, Satija R (2018) Integrating single-cell transcriptomic data across different conditions, technologies, and species. *Nat Biotechnol* 36: 411 – 420

Chung WS, Verghese PB, Chakraborty C, Joung J, Hyman BT, Ulrich JD, Holtzman DM, Barres BA (2016) Novel allele-dependent role for APOE in controlling the rate of synapse pruning by astrocytes. *Proc Natl Acad Sci U S A* 113: 10186 – 10191

Cipriani S, Ferrer I, Aronica E, Kovacs GG, Verney C, Nardelli J, Khung S, Delezoide A-L, Milenkovic I, Rasika S *et al* (2018) Hippocampal radial glial subtypes and their neurogenic potential in human fetuses and healthy and Alzheimer's disease adults. *Cereb Cortex* 28: 2458 – 2478

Clavreul S, Abdeladim L, Hernández-Garzón E, Niculescu D, Durand J, Ieng S-H, Barry R, Bonvento G, Beaurepaire E, Livet J *et al* (2019) Cortical astrocytes develop in a plastic manner at both clonal and cellular levels. *Nat Commun* 10: 4884

Costa MR, Ortega F, Brill MS, Beckervordersandforth R, Petrone C, Schroeder T, Götz M, Berninger B (2011) Continuous live imaging of adult neural stem cell division and lineage progression *in vitro*. *Development* 138: 1057 – 1068

Crespo D, Stanfield BB, Cowan WM (1986) Evidence that late-generated granule cells do not simply replace earlier formed neurons in the rat dentate gyrus. *Exp Brain Res* 62: 541 – 548

Dayer AG, Ford AA, Cleaver KM, Yassaee M, Cameron HA (2003) Short-term and long-term survival of new neurons in the rat dentate gyrus. *J Comp Neurol* 460: 563 – 572

Ehret F, Vogler S, Kempermann G (2015) A co-culture model of the hippocampal neurogenic niche reveals differential effects of astrocytes, endothelial cells and pericytes on proliferation and differentiation of adult murine precursor cells. *Stem Cell Res* 15: 514 – 521

El Waly B, Macchi M, Cayre M, Durbec P (2014) Oligodendrogenesis in the normal and pathological central nervous system. *Front Neurosci* 8: 145

Encinas JM, Michurina TV, Peunova N, Park JH, Tordo J, Peterson DA, Fishell G, Koulakov A, Enikolopov G (2011) Division-coupled astrocytic differentiation and age-related depletion of neural stem cells in the adult hippocampus. *Cell Stem Cell* 8: 566 – 579

Eroglu C, Barres BA (2010) Regulation of synaptic connectivity by glia. *Nature* 468: 223 – 231

Farioli-Vecchioli S, Mattera A, Micheli L, Ceccarelli M, Leonardi L, Saraulli D, Costanzi M, Cestari V, Rouault JP, Tirone F (2014) Running rescues defective adult neurogenesis by shortening the length of the cell cycle of neural stem and progenitor cells. *Stem Cells* 32: 1968 – 1982

Finak G, McDavid A, Yajima M, Deng J, Gersuk V, Shalek AK, Slichter CK, Miller HW, McElrath MJ, Prlic M *et al* (2015) MAST: a flexible statistical framework for assessing transcriptional changes and characterizing heterogeneity in single-cell RNA sequencing data. *Genome Biol* 16: 278

Fischer J, Beckervordersandforth R, Tripathi P, Steiner-Mezzadri A, Ninkovic J, Götz M (2011) Prospective isolation of adult neural stem cells from the mouse subependymal zone. *Nat Protoc* 6: 1981 – 1989

Franjic D, Skarica M, Ma S, Arellano JI, Tebbenkamp ATN, Choi J, Xu C, Li Q, Morozov YM, Andrijevic D *et al* (2022) Transcriptomic taxonomy and neurogenic trajectories of adult human, macaque, and pig hippocampal and entorhinal cells. *Neuron* 110: 452 – 469.e14. https://doi.org/10.1016/j.neuron.2021.10.036

Garcia A, Steiner B, Kronenberg G, Bick-Sander A, Kempermann G (2004) Age-dependent expression of glucocorticoid- and mineralocorticoid receptors on neural precursor cell populations in the adult murine hippocampus. *Aging Cell* 3: 363 – 371

Ge WP, Miyawaki A, Gage FH, Jan YN, Jan LY (2012) Local generation of glia is a major astrocyte source in postnatal cortex. *Nature* 484: 376 – 380

Gómez-Villafuertes R, Paniagua-Herranz L, Gascon S, de Agustín-Durán D, Ferreras MO, Gil-Redondo JC, Queipo MJ, Menendez-Mendez A, Pérez-Sen R, Delicado EG *et al* (2017) Live imaging followed by single cell tracking to monitor cell biology and the lineage progression of multiple neural populations. *J Vis Exp* https://doi.org/10.3791/56291

Gu L, Kleiber S, Schmid L, Nebeling F, Chamoun M, Steffen J, Wagner J, Fuhrmann M (2014) Long-term *in vivo* imaging of dendritic spines in the hippocampus reveals structural plasticity. *J Neurosci* 34: 13948 – 13953

Harris L, Rigo P, Stiehl T, Gaber ZB, Austin SHL, Masdeu MM, Edwards A, Urbán N, Marciniak-Czochra A, Guillemot F (2021) Coordinated changes in cellular behavior ensure the lifelong maintenance of the hippocampal stem cell population. *Cell Stem Cell* 28: 863 – 876.e866

Heine VM, Maslam S, Joëls M, Lucassen PJ (2004) Prominent decline of newborn cell proliferation, differentiation, and apoptosis in the aging dentate gyrus, in absence of an age-related hypothalamus-pituitary-adrenal axis activation. *Neurobiol Aging* 25: 361 – 375

Herculano-Houzel S (2014) The glia/neuron ratio: how it varies uniformly across brain structures and species and what that means for brain physiology and evolution. *Glia* 62: 1377 – 1391

Hilsenbeck O, Schwarzfischer M, Skylaki S, Schauberger B, Hoppe PS, Loeffler D, Kokkaliaris KD, Hastreiter S, Skylaki E, Filipczyk A *et al* (2016) Software tools for single-cell tracking and quantification of cellular and molecular properties. *Nat Biotechnol* 34: 703 – 706

Hirrlinger PG, Scheller A, Braun C, Quintela-Schneider M, Fuss B, Hirrlinger J, Kirchhoff F (2005) Expression of reef coral fluorescent proteins in the central nervous system of transgenic mice. *Mol Cell Neurosci* 30: 291 – 303

Hughes WL, Bond VP, Brecher G, Cronkite EP, Painter RB, Quastler H, Sherman FG (1958) Cellular proliferation in the mouse as revealed by autoradiography with tritiated thymidine. *Proc Natl Acad Sci U S A* 44: 476 – 483

Keller D, Erö C, Markram H (2018) Cell densities in the mouse brain: a systematic review. *Front Neuroanat* 12: 83

Kempermann G, Gage FH (2002) Genetic determinants of adult hippocampal neurogenesis correlate with acquisition, but not probe trial performance, in the water maze task. *Eur J Neurosci* 16: 129 – 136

Kempermann G, Kuhn HG, Gage FH (1997) Genetic influence on neurogenesis in the dentate gyrus of adult mice. *Proc Natl Acad Sci U S A* 94: 10409 – 10414

Kempermann G, Kuhn HG, Gage FH (1998) Experience-induced neurogenesis in the senescent dentate gyrus. *J Neurosci* 18: 3206 – 3212

Kempermann G, Song H, Gage FH (2015) Neurogenesis in the Adult Hippocampus. *Cold Spring Harb Perspect Biol* 7: a018812 . https://doi.org/10.1101/cshperspect.a018812

Kuhn HG, Dickinson-Anson H, Gage FH (1996) Neurogenesis in the dentate gyrus of the adult rat: age-related decrease of neuronal progenitor proliferation. *J Neurosci* 16: 2027 – 2033

Lagace DC, Whitman MC, Noonan MA, Ables JL, DeCarolis NA, Arguello AA, Donovan MH, Fischer SJ, Farnbauch LA, Beech RD *et al* (2007) Dynamic contribution of nestin-expressing stem cells to adult neurogenesis. *J Neurosci* 27: 12623 – 12629

Lee SW, Clemenson GD, Gage FH (2012) New neurons in an aged brain. *Behav Brain Res* 227: 497 – 507

Li X, Newbern JM, Wu Y, Morgan-Smith M, Zhong J, Charron J, Snider WD (2012) MEK is a key regulator of gliogenesis in the developing brain. *Neuron* 75: 1035 – 1050

Lie D-C, Colamarino SA, Song H-J, Désiré L, Mira H, Consiglio A, Lein ES, Jessberger S, Lansford H, Dearie AR *et al* (2005) Wnt signalling regulates adult hippocampal neurogenesis. *Nature* 437: 1370 – 1375

Lukassen S, Bosch E, Ekici AB, Winterpacht A (2018) Characterization of germ cell differentiation in the male mouse through single-cell RNA sequencing. *Sci Rep* 8: 6521

Luo K (2017) Signaling cross talk between TGF-β/Smad and other signaling pathways. *Cold Spring Harb Perspect Biol* 9: a022137

Mabie PC, Mehler MF, Marmur R, Papavasiliou A, Song Q, Kessler JA (1997) Bone morphogenetic proteins induce astroglial differentiation of oligodendroglial-astroglial progenitor cells. *J Neurosci* 17: 4112 – 4120

Mathews EA, Morgenstern NA, Piatti VC, Zhao C, Jessberger S, Schinder AF, Gage FH (2010) A distinctive layering pattern of mouse dentate granule cells is generated by developmental and adult neurogenesis. *J Comp Neurol* 518: 4479 – 4490

Mi H, Muruganujan A, Huang X, Ebert D, Mills C, Guo X, Thomas PD (2019) Protocol update for large-scale genome and gene function analysis with the PANTHER classification system (v.14.0). *Nat Protoc* 14: 703 – 721

Miller FD, Gauthier AS (2007) Timing is everything: making neurons versus glia in the developing cortex. *Neuron* 54: 357 – 369

Ming GL, Song H (2011) Adult neurogenesis in the mammalian brain: significant answers and significant questions. *Neuron* 70: 687 – 702

Mira H, Andreu Z, Suh H, Lie DC, Jessberger S, Consiglio A, San Emeterio J, Hortigüela R, Marqués-Torrejón MÁ, Nakashima K *et al* (2010) Signaling through BMPR-IA regulates quiescence and long-term activity of neural stem cells in the adult hippocampus. *Cell Stem Cell* 7: 78 – 89

Moreno-Jiménez EP, Flor-García M, Terreros-Roncal J, Rábano A, Cafini F, Pallas-Bazarra N, Ávila J, Llorens-Martín M (2019) Adult hippocampal neurogenesis is abundant in neurologically healthy subjects and drops sharply in patients with Alzheimer's disease. *Nat Med* 25: 554 – 560

Nakamura T, Colbert MC, Robbins J (2006) Neural crest cells retain multipotential characteristics in the developing valves and label the cardiac conduction system. *Circ Res* 98: 1547 – 1554

Nicola Z, Fabel K, Kempermann G (2015) Development of the adult neurogenic niche in the hippocampus of mice. *Front Neuroanat* 9: 53

Nolte C, Matyash M, Pivneva T, Schipke CG, Ohlemeyer C, Hanisch UK, Kirchhoff F, Kettenmann H (2001) GFAP promoter-controlled EGFP-expressing transgenic mice: a tool to visualize astrocytes and astrogliosis in living brain tissue. *Glia* 33: 72 – 86

Ohlig S, Clavreul S, Thorwirth M, Simon-Ebert T, Bocchi R, Ulbricht S, Kannayian N, Rossner M, Sirko S, Smialowski P *et al* (2021) Molecular diversity of diencephalic astrocytes reveals adult astrogenesis regulated by Smad4. *EMBO J* 40(21): e107532

Olariu A, Cleaver KM, Cameron HA (2007) Decreased neurogenesis in aged rats results from loss of granule cell precursors without lengthening of the cell cycle. *J Comp Neurol* 501: 659 – 667

Ortega F, Berninger B, Costa MR (2013) Primary culture and live imaging of adult neural stem cells and their progeny. *Methods Mol Biol* 1052: 1 – 11

Ortega F, Costa MR (2016) Live imaging of adult neural stem cells in rodents. *Front Neurosci* 10: 78

Overall RW, Walker TL, Leiter O, Lenke S, Ruhwald S, Kempermann G (2013) Delayed and transient increase of adult hippocampal neurogenesis by physical exercise in DBA/2 mice. *PLoS One* 8: e83797

Paniagua-Herranz L, Gómez-Villafuertes R, de Agustín-Durán D, Gascón S, Pérez-Sen R, Delicado EG, Miras-Portugal MT, Ortega F (2020) Time-lapse video microscopy and single cell tracking to study neural cell behavior *in vitro*. *Methods Mol Biol* 2150: 183 – 194

Patzke N, Spocter MA, Karlsson KÆ, Bertelsen MF, Haagensen M, Chawana R, Streicher S, Kaswera C, Gilissen E, Alagaili AN *et al* (2015) In contrast to many other mammals, cetaceans have relatively small hippocampi that appear to lack adult neurogenesis. *Brain Struct Funct* 220: 361 – 383

Perea G, Araque A (2007) Astrocytes potentiate transmitter release at single hippocampal synapses. *Science* 317: 1083 – 1086

Pilz GA, Bottes S, Betizeau M, Jörg DJ, Carta S, Simons BD, Helmchen F, Jessberger S (2018) Live imaging of neurogenesis in the adult mouse hippocampus. *Science* 359: 658 – 662

Pleasure SJ, Collins AE, Lowenstein DH (2000) Unique expression patterns of cell fate molecules delineate sequential stages of dentate gyrus development. *J Neurosci* 20: 6095 – 6105

van Praag H (2008) Neurogenesis and exercise: past and future directions. *Neuromolecular Med* 10: 128 – 140

van Praag H, Christie BR, Sejnowski TJ, Gage FH (1999a) Running enhances neurogenesis, learning, and long-term potentiation in mice. *Proc Natl Acad Sci* 96: 13427 – 13431

van Praag H, Kempermann G, Gage FH (1999b) Running increases cell proliferation and neurogenesis in the adult mouse dentate gyrus. *Nat Neurosci* 2: 266 – 270

van Praag H, Shubert T, Zhao C, Gage FH (2005) Exercise enhances learning and hippocampal neurogenesis in aged mice. *J Neurosci* 25: 8680 – 8685

Rickmann M, Amaral DG, Cowan WM (1987) Organization of radial glial cells during the development of the rat dentate gyrus. *J Comp Neurol* 264: 449 – 479

Schindelin J, Arganda-Carreras I, Frise E, Kaynig V, Longair M, Pietzsch T, Preibisch S, Rueden C, Saalfeld S, Schmid B *et al* (2012) Fiji: an open-source platform for biological-image analysis. *Nat Methods* 9: 676 – 682

Schlessinger AR, Cowan WM, Gottlieb DI (1975) An autoradiographic study of the time of origin and the pattern of granule cell migration in the dentate gyrus of the rat. *J Comp Neurol* 159: 149 – 175

Schneider J, Karpf J, Beckervordersandforth R (2019) Role of astrocytes in the neurogenic niches. *Methods Mol Biol* 1938: 19 – 33

Schroeder T (2008) Imaging stem-cell-driven regeneration in mammals. *Nature* 453: 345 – 351

Seki T (2002) Expression patterns of immature neuronal markers PSA-NCAM, CRMP-4 and NeuroD in the hippocampus of young adult and aged rodents. *J Neurosci Res* 70: 327 – 334

Seki T, Hori T, Miyata H, Maehara M, Namba T (2019) Analysis of proliferating neuronal progenitors and immature neurons in the human hippocampus surgically removed from control and epileptic patients. *Sci Rep* 9: 18194

Seri B, García-Verdugo JM, McEwen BS, Alvarez-Buylla A (2001) Astrocytes give rise to new neurons in the adult mammalian hippocampus. *J Neurosci* 21: 7153 – 7160

Shen Z, Lin Y, Yang J, Jörg DJ, Peng Y, Zhang X, Xu Y, Hernandez L, Ma J, Simons BD *et al* (2021) Distinct progenitor behavior underlying neocortical gliogenesis related to tumorigenesis. *Cell Rep* 34: 108853

Shetty AK, Hattiangady B, Shetty GA (2005) Stem/progenitor cell proliferation factors FGF-2, IGF-1, and VEGF exhibit early decline during the course of aging in the hippocampus: role of astrocytes. *Glia* 51: 173 – 186

Singhal G, Morgan J, Jawahar MC, Corrigan F, Jaehne EJ, Toben C, Manavis J, Hannan AJ, Baune BT (2020) Duration of environmental enrichment determines astrocyte number and cervical lymph node T lymphocyte proportions but not the microglial number in middle-aged C57BL/6 mice. *Front Cell Neurosci* 14: 57

Sock E, Wegner M (2019) Transcriptional control of myelination and remyelination. *Glia* 67: 2153 – 2165

Song H, Stevens CF, Gage FH (2002) Astroglia induce neurogenesis from adult neural stem cells. *Nature* 417: 39 – 44

Song J, Christian KM, Ming GL, Song H (2012) Modification of hippocampal circuitry by adult neurogenesis. *Dev Neurobiol* 72: 1032 – 1043

Sorrells SF, Paredes MF, Cebrian-Silla A, Sandoval K, Qi D, Kelley KW, James D, Mayer S, Chang J, Auguste KI *et al* (2018) Human hippocampal neurogenesis drops sharply in children to undetectable levels in adults. *Nature* 555: 377 – 381

Spalding K, Bergmann O, Alkass K, Bernard S, Salehpour M, Huttner H, Boström E, Westerlund I, Vial C, Buchholz B *et al* (2013) Dynamics of hippocampal neurogenesis in adult humans. *Cell* 153: 1219 – 1227

Srinivas S, Watanabe T, Lin C-S, William CM, Tanabe Y, Jessell TM, Costantini F (2001) Cre reporter strains produced by targeted insertion of EYFP and ECFP into the ROSA26 locus. *BMC Dev Biol* 1: 4

Stipursky J, Francis D, Dezonne RS, Bérgamo de Araújo AP, Souza L, Moraes CA, Alcantara Gomes FC (2014) TGF-β1 promotes cerebral cortex radial glia-astrocyte differentiation *in vivo*. *Front Cell Neurosci* 8: 393

Stuart T, Butler A, Hoffman P, Hafemeister C, Papalexi E, Mauck 3rd WM, Hao Y, Stoeckius M, Smibert P, Satija R (2019) Comprehensive integration of single-cell data. *Cell* 177: 1888 – 1902.e1821

Suh H, Consiglio A, Ray J, Sawai T, D'Amour KA, Gage FH (2007) *In vivo* fate analysis reveals the multipotent and self-renewal capacities of

Sox2+ neural stem cells in the adult hippocampus. *Cell Stem Cell* 1: 515 – 528

Sultan S, Li L, Moss J, Petrelli F, Cassé F, Gebara E, Lopatar J, Pfrieger F, Bezzi P, Bischofberger J *et al* (2015) Synaptic integration of adult-born hippocampal neurons is locally controlled by astrocytes. *Neuron* 88: 957 – 972

Suzuki A, Stern SA, Bozdagi O, Huntley GW, Walker RH, Magistretti PJ, Alberini CM (2011) Astrocyte-neuron lactate transport is required for long-term memory formation. *Cell* 144: 810 – 823

Takeuchi A, Takahashi Y, Iida K, Hosokawa M, Irie K, Ito M, Brown JB, Ohno K, Nakashima K, Hagiwara M (2020) Identification of Qk as a glial precursor cell marker that governs the fate specification of neural stem cells to a glial cell lineage. *Stem Cell Reports* 15: 883 – 897

Tien A-C, Tsai H-H, Molofsky AV, McMahon M, Foo LC, Kaul A, Dougherty JD, Heintz N, Gutmann DH, Barres BA *et al* (2012) Regulated temporal-spatial astrocyte precursor cell proliferation involves BRAF signalling in mammalian spinal cord. *Development* 139: 2477 – 2487

Tobin MK, Musaraca K, Disouky A, Shetti A, Bheri A, Honer WG, Kim N, Dawe RJ, Bennett DA, Arfanakis K *et al* (2019) Human hippocampal neurogenesis persists in aged adults and Alzheimer's disease patients. *Cell Stem Cell* 24: 974 – 982.e973

Ulivi AF, Castello-Waldow TP, Weston G, Yan L, Yasuda R, Chen A, Attardo A (2019) Longitudinal two-photon imaging of dorsal hippocampal CA1 in live mice. *J Vis Exp* https://doi.org/10.3791/59598

Urbán N, Guillemot F (2014) Neurogenesis in the embryonic and adult brain: same regulators, different roles. *Front Cell Neurosci* 8: 396

Verkhratsky A, Nedergaard M (2018) Physiology of Astroglia. *Physiol Rev* 98: 239 – 389

Verkhratsky A, Parpura V (2016) Astrogliopathology in neurological, neurodevelopmental and psychiatric disorders. *Neurobiol Dis* 85: 254 – 261

Walter J, Keiner S, Witte OW, Redecker C (2011) Age-related effects on hippocampal precursor cell subpopulations and neurogenesis. *Neurobiol Aging* 32: 1906 – 1914

Williamson LL, Chao A, Bilbo SD (2012) Environmental enrichment alters glial antigen expression and neuroimmune function in the adult rat hippocampus. *Brain Behav Immun* 26: 500 – 510

Woodbury ME, Freilich RW, Cheng CJ, Asai H, Ikezu S, Boucher JD, Slack F, Ikezu T (2015) miR-155 is essential for inflammation-induced hippocampal neurogenic dysfunction. *J Neurosci* 35: 9764 – 9781

Yamaguchi M, Saito H, Suzuki M, Mori K (2000) Visualization of neurogenesis in the central nervous system using nestin promoter-GFP transgenic mice. *NeuroReport* 11: 1991 – 1996

Zhu X, Hill RA, Dietrich D, Komitova M, Suzuki R, Nishiyama A (2011) Age-dependent fate and lineage restriction of single NG2 cells. *Development* 138: 745 – 753